

**COMPUTATIONAL DESIGN OF ADVANCED AEROTURBINE MATERIALS:  
NOBURNIUM CYBERALLOY**

**AFOSR GRANT F49620-01-1-0529**

G.B. Olson, A.J. Freeman, M. Asta and G. Ghosh  
Materials Technology Laboratory, Northwestern University

J. Perepezko  
U. Wisconsin-Madison

M. Eberhart  
Colorado School of Mines

C. Woodward  
UES/WPAFB

**DISTRIBUTION STATEMENT A**  
Approved for Public Release  
Distribution Unlimited

**Abstract**

Under the AFOSR-MEANS initiative, an optimal combination of electronic-level first-principles calculations and efficient experimentation addresses the accelerated design and development of a new class of Nb-based aeroturbine superalloys.

**Research Objectives**

The objective of this multi-institutional, multidisciplinary effort is to develop optimal strategies for the integration of theory and efficient experimentation for the accelerated design and development of advanced structural materials, using the example of Nb-based superalloys combining oxidation resistance, creep strength and ductility for future aeroturbine blade applications operating at 1300C and above.

**Approach**

Based on experience in Ni-based superalloys, the primary microstructural concept is a metallic matrix alloy solution, strengthened by a fine dispersion of low-misfit coherent aluminide precipitates incorporating low diffusivity components for coarsening resistance. The precipitates contribute both creep strength and a source of Al for oxidation resistance via  $Al_2O_3$  passivation. Matrix solution requirements include low O solubility and a high diffusivity ratio of Al to O to maintain passivation.

**Progress**

Our progress has been summarized in an invited overview paper for a recent international symposium on Nb alloys [1]. Guided by phase stability predictions using the FLAPW method, designed model alloys allowed rapid experimental determination of equilibrium tie-tetrahedra in the quaternary Nb-Pd-Hf-Al system bounding the desired Nb-Pd<sub>2</sub>HfAl-PdAl three phase field of interest for coherent aluminide dispersion strengthened alloys [2], and alloys were then prepared demonstrating desired finely dispersed microstructures. Extensive FLAPW calculations then

assessed the solution thermodynamics and molar volume behavior of the multicomponent (Pd,Pt)<sub>2</sub>(Hf,Zr)Al Heusler phase for improved control of phase stability and interphase misfit, with predicted component intersolubilities validated by selected diffusion couple experiments. BCC solution thermodynamics has been evaluated via a cluster expansion description using the VASP method [2,3]. Using a simple model of O solubility and a preliminary mobility database for prediction of O and Al diffusivities, a team of students in an undergraduate materials design class [4] integrated our models and databases in the theoretical design of oxidation resistant Nb alloys with a combination of Pd<sub>2</sub>HfAl and PdAl phases dispersed in a multicomponent BCC Nb-based matrix. Evaluation of their prototype alloys demonstrated predicted microstructures and a substantial level of protective oxide film formation, although predicted Al<sub>2</sub>O<sub>3</sub> passivation was not achieved. The student project won first prize in the 2004 TMS-AIME undergraduate design competition.

Based on the preliminary design evaluations, efforts in the past year have emphasized improvement in the mobility models and databases to more precisely control the transport properties governing protective oxide film formation. As a heuristic device for component selection, ADF cluster calculations have assessed the electronic charge density in the octahedral interstitial sites surrounding substitutional atoms in BCC Nb giving the behavior summarized in Figure 1a. It was anticipated that components increasing the charge density will promote lower O solubility while those giving a dramatic decrease in charge density will promote lower O diffusivity through a solution thermodynamic "trapping" effect. Based on this assessment a series of binary alloys with 10<sup>a</sup>% solute were oxidized at 1300C and O diffusion fields were measured by microhardness profiles. The O diffusivities thus measured are summarized in Figure 1b, giving a pattern which is strikingly similar to the relative charge density predictions of Figure 1a. The components Al, Ti, Hf, Y and Pd are shown to strongly reduce O diffusivity with Al showing an order-of-magnitude reduction. The components Al and Hf were then selected for VASP calculations of Nb-X-O ternary solution thermodynamics summarized in Figure 2. The predicted Hf-O chemical attraction is confirmed. For the case of Al which contracts the BCC Nb lattice, an unrelaxed calculation supports a strong Al-O chemical attraction in the nearest octahedral site, but a structurally relaxed calculation shows an overall repulsive interaction attributed to a dominance of elastic interaction in the contracted lattice. The experimentally observed reduction of O diffusivity by Al is thus tentatively attributed to an effect on atomic mobility rather than solution thermodynamics and calculations exploring this are underway. For substitutional diffusion, available measured atomic mobilities in Nb are supplemented by theoretical predictions through a combination of the semi-empirical model of Neumann and Tuijn (*Solid State Phenomena*, Vol. 88, 2002) and preliminary first-principles calculations by Woodward [1]. These models are combined with diffusion couple measurements to define the effect of 10<sup>a</sup>% binary solute additions on the impurity diffusivity of Al at 1300C summarized in Figure 3. The solutes Cr, Pd, Ti, Hf and W are found to enhance Al diffusivity, with the effect of Cr approaching an order of magnitude. Also shown for comparison is the chemical diffusivity of Al at 10<sup>a</sup>% concentration, showing an enhancement by over 2 orders of magnitude.

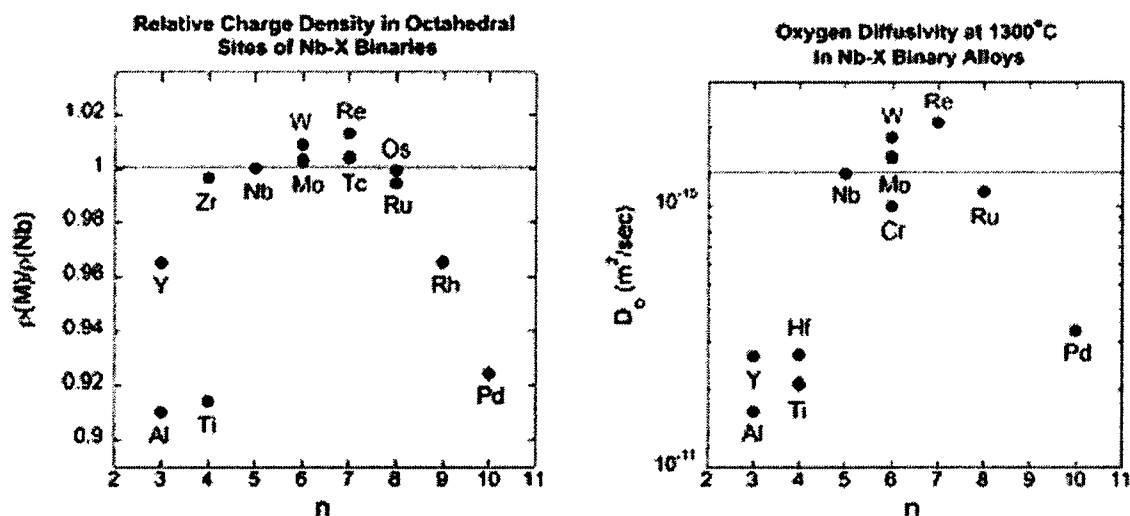


Figure 1 Correlation of calculated relative charge densities in octahedral sites of Nb-X alloys with measured O diffusivities. (a) Calculated charge densities, (b) Measured relative O diffusivities for  $10^{a/oX}$  at 1300C.

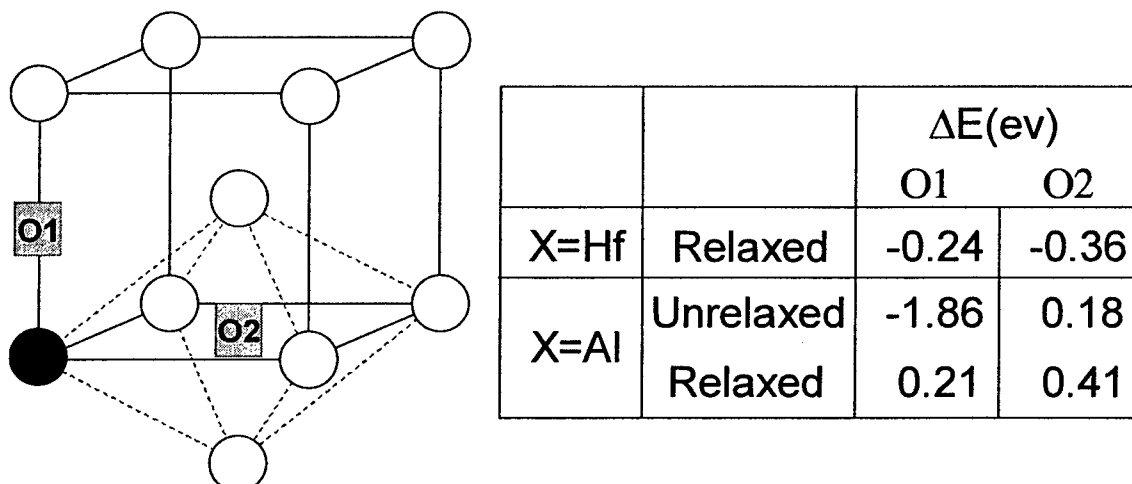


Figure 2 Calculated solute-oxygen binding energies for Hf and Al in BCC Nb.

Guided by the diffusivity behaviors, Al solubilities in BCC Nb at 1300C in Nb-Al-X ternary systems were examined using literature phase diagrams for Cr, Ti and Zr, and our own first-principles calculations for Hf [1]. The latter case shows the highest Al solubility, reaching  $21^{a/oAl}$  at  $34^{a/oHf}$ . Preparation of this composition revealed a slightly lower Al solubility of  $16^{a/o}$  associated with formation of a  $Nb_2Al$  dispersion. Although our diffusivity models predict that necessary relative diffusivities of O and Al are satisfied to allow  $Al_2O_3$  passivation, oxidation of the alloy at 1300C produced the complex oxide scale shown in Figure 4 where an unusually compact and adherent  $(Nb_{0.75}Al_{0.17}Hf_{0.06})_2O_5$  external layer forms above a parabolically-growing two-phase rutile-type scale composed of  $NbAlO_4$  and  $(Hf,Nb,Al)O_2$ . We

conclude that the desired  $\text{Al}_2\text{O}_3$  formation is in this case thermodynamically prevented by an unanticipated high stability of the  $\text{NbAlO}_4$  oxide. Nonetheless the complex scale shows a parabolic growth constant of  $k_p=0.12\text{mg}^2/\text{cm}^4\text{-sec}$  which meets the recession rate over 2000 hrs corresponding to the IHPTET Phase III goals for a 1300C aeroturbine blade alloy. Investigation of the 1300C oxidation behavior of thermodynamically compatible protective aluminide bondcoats for such an alloy show a lower parabolic rate constant by 4.3X for  $\text{Pd}_2\text{HfAl}$  associated with formation of an adherent  $\text{Al}_2\text{O}_3+\text{HfO}_2+\text{PdO}_2$  oxide layer, and demonstrate compact  $\text{Al}_2\text{O}_3$  formation on  $\text{PdAl}$ .

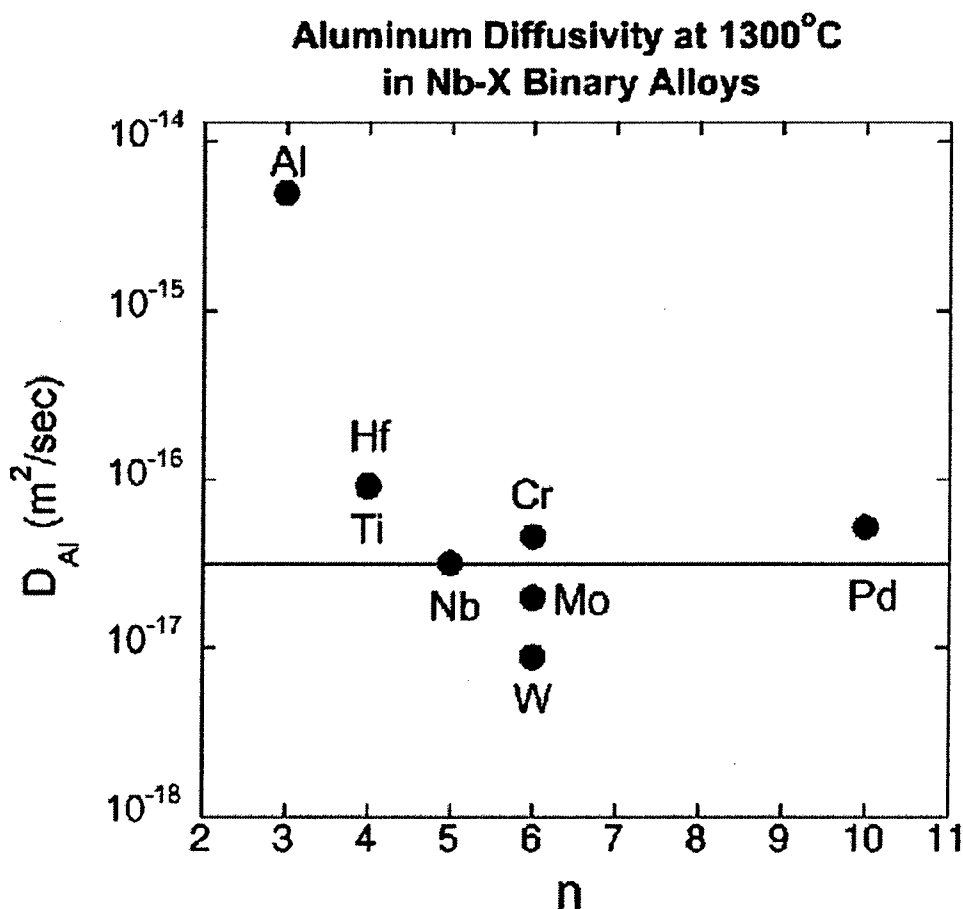


Figure 3 Measured Al impurity diffusivity at 1300C for Nb-X alloys referenced to  $10^2/\text{oX}$ . Al point represents Al chemical diffusivity at  $10^2/\text{oAl}$ .

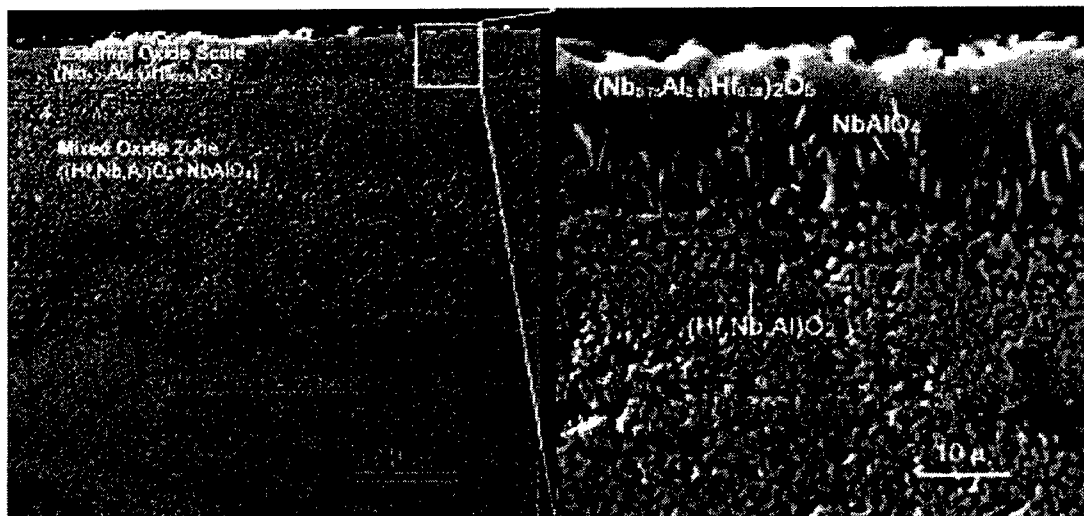


Figure 4 Oxide scale formed on two-phase BCC+Nb<sub>2</sub>Al Nb-34<sup>a</sup>/oHf-21<sup>a</sup>/oAl at 1300C. Adherent multiphase scale gives an oxidation parabolic rate constant of  $k_p=0.12 \text{ mg}^2/\text{cm}^4\text{-sec}$ .

To further enhance intrinsic alloy oxidation resistance, a broader survey has been conducted of fast-diffusing components which can promote slow growing oxides of sufficient thermodynamic stability to displace the competing NbAlO<sub>4</sub>. Supporting candidate intermetallic phases thermodynamically compatible with Nb have been identified by FLAPW stability calculations, compound melting point measurements and validated phase relations. Oxidation studies of promising alloy prototypes are underway, with preliminary results confirming predicted oxide films with an associated 2 orders of magnitude reduction in  $k_p$ .

#### Acknowledgment/Disclaimer

This work was sponsored by the Air Force Office of Scientific Research, USAF, under grant number F49620-01-1-0529, with additional support from Reference Metals Company, Inc., and computer time grants from San Diego Supercomputing Center, ERDC and the DoD High Performance Computing Modernization Program at the Aeronautical Systems Center – Major Shared Resource Center. The views and conclusions contained herein are those of the authors and should not be interpreted as necessarily representing the official policies or endorsements, either expressed or implied, of the Air Force Office of Scientific Research or the U.S. Government.

#### Personnel Supported

M. Asta	Professor, Northwestern University
D. Bryan	Graduate Student, Northwestern University
M. Eberhart	Professor, Colorado School of Mines
A.J. Freeman	Professor, Northwestern University
G. Ghosh	Research Asst Professor, Northwestern University
M. Kim	Postdoc, Northwestern University
S. Kim	Graduate Student, University of Wisconsin-Madison

A. Misra	Graduate Student, Northwestern University
G.B. Olson	Professor, Northwestern University
J. Perepezko	Professor, University of Wisconsin-Madison
A. van de Walle	Postdoc, Northwestern University

#### **Publications**

1. G. B. Olson, A. J. Freeman, P. W. Voorhees, G. Ghosh, J. Perepezko, M. Eberhart, and C. Woodward, "Quest for Noburnium: 1300C Cyberalloy," *International Symposium on Niobium for High Temperature Applications*, eds. Y-W. Kim and T. Carneiro, (Warrendale PA, TMS, 2004) 113-122.
2. A. Misra, R. Bishop, G. Ghosh and G.B. Olson, "Phase Relations in Prototype Nb-Pd-Hf-Al Alloys," *Metallurgical and Materials Transactions A*, 34A (2003), 1771-1781.
3. G. Ghosh, A. van de Walle, M. Asta and G. B. Olson, "Phase Stability of the Hf-Nb System: From First-Principles to CALPHAD," *CALPHAD*, 26 (4) (2002), 491-511.
4. E. Altinoglu, J. Bolos and N. Colligan, "Noburnium: Oxidation Resistant Nb Superalloy," Northwestern University, MSc 390 Materials Design project report (May 2003); 2004 TMS-AIME Undergraduate Design Competition winner.

#### **Awards Received**

2004 TMS-AIME Undergraduate Design Competition, First Place – N. Altinoglu, J. Bolos and N. Colligan; Project Titled: "Noburnium: Oxidation Resistant Nb Superalloy."

2004 SMD/TMS-AIME Distinguished Scientist/Engineer Award – G. B. Olson.

#### **Transitions**

Based on the success of this research, our materials design spinoff company, QuesTek Innovations LLC, has initiated a NASA-sponsored project on design of Nb based alloys for deep space exploration applications.

## APPENDIX A

### ATOMIC SELECTION FOR ENHANCED OXIDATION RESISTANCE

To overcome the thermodynamic stability of the competing rutile-type  $\text{NbAlO}_4$  oxide while satisfying kinetic constraints, thermodynamic and kinetic atomic selection criteria were devised for a broader survey of components and phases for enhanced oxidation resistance of Nb based alloys. The four-dimensional survey is summarized by the Ashby-type selection cross plots in Figure A1. The plot at the left represents the equilibrium thermodynamic parameters of oxide free energy of formation and Pilling-Bedworth (P-B) ratio relative to Nb, while the plot at the right represents 1300C kinetic parameters of oxide scale parabolic rate constant and relative diffusivity in Nb of the corresponding metal solute. Preferred properties in the left plot lie at the upper left, while preferred properties in the right plot lie at the lower right. Using a lower bound estimate of the  $\Delta G_f$  for  $\text{NbAlO}_4$  based on its component  $\text{Al}_2\text{O}_3$ , and  $\text{Nb}_2\text{O}_5$  oxides, the thermodynamic plot at the left shows that  $\text{Y}_2\text{O}_3$  offers desired high stability with the same P-B ratio as the rutile oxides, and mixed  $\text{Al}_2\text{O}_3$ - $\text{Y}_2\text{O}_3$  oxides such as YAG (Yttrium-Aluminum Garnet) offer a good compromise between stability and P-B ratio. Bracketing relative component diffusivities of mixed oxides by their corresponding atomic constituents, the kinetic plot at the right shows that  $\text{Y}_2\text{O}_3$  also offers the advantage of the high diffusivity of Y in Nb while providing a low  $k_p$  equivalent to  $\text{Cr}_2\text{O}_3$ . The well known low transport properties of YAG offer promise of exceptionally low  $k_p$ , but the relative diffusivity will be compromised by the slower diffusion of Al. These considerations identify  $\text{Y}_2\text{O}_3$  and YAG as preferred oxide scales with the prospect of alloys that could take advantage of the high diffusivity of Y to initially passivate with  $\text{Y}_2\text{O}_3$  followed by longer time passivation by slower growing YAG.

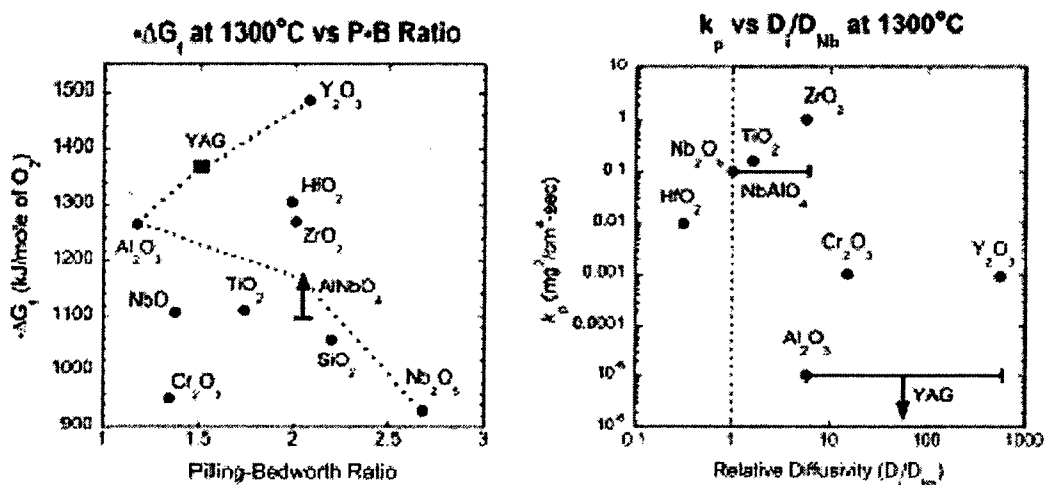


Figure A1 Atomic Selection Parametric Cross Plots.

A challenge to the incorporation of Y in our alloys is the low solubility of Y in Nb and the relatively low melting point of Y compounds. Of the binary Y-Al compounds,  $Al_2Y$  offers the highest melting point (1485C) and the nearest stoichiometry to that of YAG. Our experiments show however that it reacts with Nb to form a Nb aluminide and the lower melting point  $AlY$ . A literature survey of Y compounds identified those with Pt group metals to be the most stable. Promising Y-Al ternary compounds were then fabricated and their melting points measured by high-temperature DTA. As summarized in Table 1 the equiatomic PtYAl is uniquely distinguished by its melting point above 1500C meeting a primary requirement for our high temperature alloys. Table 2 summarizes our FLAPW calculation of its heat of formation which is greater than -100kJ/mol-atom, exceeding that of our previously studied Heusler compounds. Consistent with this high stability, phase relations measured in model alloys confirm compatibility with Nb. Incorporation into design of a multicomponent alloy optimized for necessary transport properties gives the 1300C microstructure shown at the left in Figure A2, where PtYAl is the predominant dispersed phase. Oxidation at 1300C confirms formation of the predicted stable  $Y_2O_3$  outer scale shown at the right. The scale thickness corresponds to a reduction in oxidation rate constant  $k_p$  by two orders of magnitude. Below the  $Y_2O_3$  scale is a mixed layer of  $Al_2O_3+Y_2O_3$  with a dispersion of Pt. Longer time oxidation behavior and the kinetic conditions for conversion of the  $Al_2O_3+Y_2O_3$  layer to the desired stable YAG are under investigation. Our successful predictive design of a  $Y_2O_3$  passivating metallic matrix alloy represents a significant breakthrough in the development of oxidation resistant Nb-based superalloys.

Table 1. Measured melting points of ternary Y-Al compounds

Phase	Crystal Structure	Melting Point
PtYAl	TiNiSi	1580C
PdYAl	TiNiSi	1160C
Pt <sub>2</sub> YAl	2 Phase	1120C
Pd <sub>2</sub> YAl	Na <sub>3</sub> As	890C

Table 2. Computed Compound Heats of Formation-FLAPW

Compound	Structure	Method	$\Delta H_f$ , kJ/mol-atom
PtYAl		GGA	-109.85
		LDA	-111.78
Pt <sub>2</sub> HfAl	L2 <sub>1</sub>	LDA	-94.44
Pt <sub>2</sub> ZrAl	L2 <sub>1</sub>	LDA	-93.47
Pd <sub>2</sub> HfAl	L2 <sub>1</sub>	LDA	-79.98
		LDA	-79.02

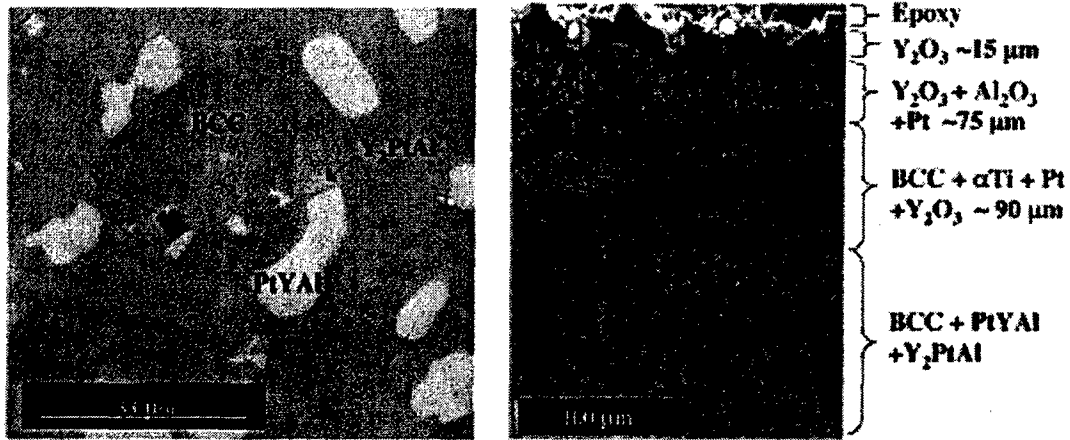


Figure A2 Alloy and Oxide Scale Microstructures in Design Prototype.

**QUEST FOR NOBURNIUM: 1300C CYBERALLOY**G. B. Olson<sup>1</sup>, A. J. Freeman<sup>1</sup>, P. W. Voorhees<sup>1</sup>, G. Ghosh<sup>1</sup>, J. Perepezko<sup>2</sup>, M. Eberhart<sup>3</sup>,  
and C. Woodward<sup>1,4</sup><sup>1</sup>Northwestern University  
2220 Campus Drive, Evanston, IL, 60208-3108, USA<sup>2</sup>University of Wisconsin  
1509 University Avenue, Madison, WI, 53706, USA,<sup>3</sup>Colorado School of Mines  
Golden, CO, USA, 80401, USA<sup>4</sup>Wright-Patterson AFB, OH, 45433, USA

Keywords: Materials Design, Quantum Engineering

**Abstract**

A multi-institutional, multidisciplinary project addresses optimal integration of computational design and efficient experimentation for the accelerated design and development of high performance materials using the example of Nb-based superalloys combining oxidation resistance, creep strength and ductility for aeroturbine applications operating at 1300°C and above. Integrated within a systems engineering framework, the effort tests the limits of ab-initio quantum mechanical methods to accelerate assessment of thermodynamic and kinetic databases enabling comprehensive predictive design of multicomponent multiphase microstructures as dynamic systems. Based on established principles underlying Ni base superalloys, the central microstructural concept is a dispersion strengthened system in which coherent cubic aluminide phases provide both creep strengthening and a source of Al for Al<sub>2</sub>O<sub>3</sub> passivation enabled by a Nb-based BCC alloy matrix with required transport and oxygen solubility behaviors. A combination of FLAPW all-electron and VASP pseudopotential calculations assess thermodynamic and molar volume behaviors of L<sub>21</sub> Pd<sub>2</sub>HfAl and B2 PdAl based intermetallics as well as BCC Nb-based solutions. Toward an optimal balance of phase stability and interphase misfit, the L<sub>21</sub> phase assessment has been extended to the (Pd,Pt)<sub>2</sub>(Hf,Zr,Nb)Al system with validation by diffusion couple experiments. To identify slow diffusing species to enhance dispersion coarsening resistance, quantum methods predict an activation energy for Re diffusion in Nb 50% higher than that for Mo in Nb. Employing the DICTRA system, a multicomponent diffusivity database is developed for substitutional alloying elements and interstitial oxygen to enhance the diffusivity ratio of Al to O for promotion of Al<sub>2</sub>O<sub>3</sub> passivation. To minimize O solubility, quantum bond topology calculations show trends in interstitial site charge density supporting a dependence of O chemical potential on solution e/a ratio. Integrating the databases and models thusfar developed, a team of students in an undergraduate Materials Design class has performed theoretical designs of 7 component dispersion strengthened alloys with matrix transport and solubility properties supporting feasibility of Al<sub>2</sub>O<sub>3</sub> passivation at 1300°C.

**Research Objectives**

In support of the US Air Force MEANS (Materials Engineering for Affordable New Systems) program,

the objective of this multidisciplinary collaboration is to develop optimal strategies for the integration of theory and efficient experimentation for the accelerated design and development of advanced structural materials, using the example of Nb-based superalloys combining oxidation resistance, creep strength and ductility for future aeroturbine blade applications operating at 1300°C and above.

### Approach

Building on demonstrated successes in computational materials design [1], a central theme of the AF-MEANS initiative is the acceleration of the full materials design, development and qualification cycle. This requires not only the extension of materials design tools to process optimization, scaleup, and control of variation, but also the development of new strategies for more efficient integration of theory and experiment. Our systems engineering approach to materials design is represented by Figure 1, summarizing the process-structure-property connections governing the behavior of a multilevel-structured coated Nb-based superalloy system. While the total system integrates compatible thermal barrier and bondcoat subsystems, our initial research has focused on predictive design of the underlying precipitation-strengthened alloy. The specific tools employed in this effort explore the limits of modern quantum engineering methods based on total energy calculations.

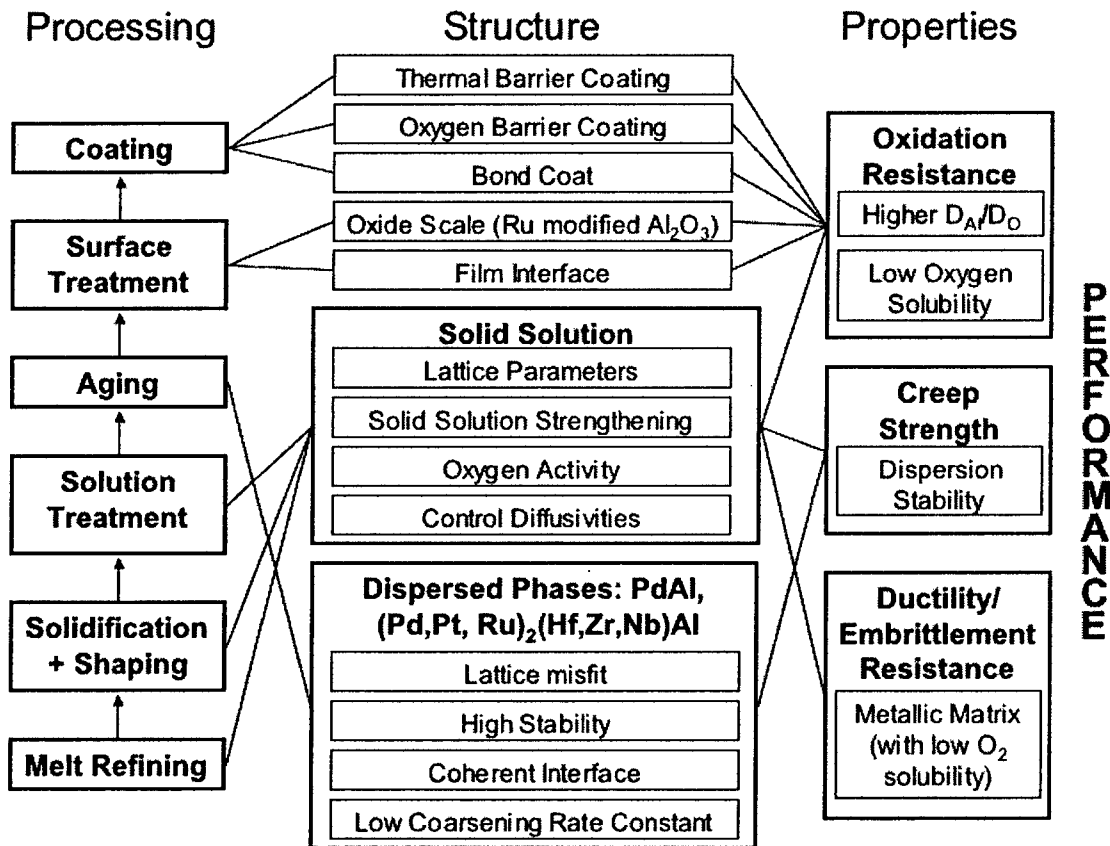


Figure 1. System chart representing coated Nb-based superalloy for aeroturbine blade applications.

Based on experience in Ni-based superalloys, the primary microstructural concept is a metallic matrix alloy solution, strengthened by a fine dispersion of low-misfit coherent aluminide precipitates incorporating low diffusivity components for coarsening resistance. The precipitates contribute both creep strength and a source of Al for oxidation resistance via  $\text{Al}_2\text{O}_3$  passivation. As predicted by Wagner's analysis [2] the critical alloy Al content,  $N_{\text{Al}}^{\text{crit}}$ , for formation of a stable passivating  $\text{Al}_2\text{O}_3$  film is expressed by:

$$N_{\text{Al}}^{\text{crit}} = A \left( \frac{N_{\text{O}}^{(s)} D_{\text{O}}}{D_{\text{Al}}} \right)^{1/2} \quad (1)$$

where A is a constant,  $N_{\text{O}}^{(s)}$  is the oxygen solubility in the alloy matrix, and  $D_{\text{O}}$  and  $D_{\text{Al}}$  are the diffusivities of oxygen and aluminum, respectively. Matrix solution requirements thus include low O solubility and a high diffusivity ratio of Al to O to maintain passivation.

### Results and Discussion

As summarized in Table 1 [3,4], a survey of potential aluminide phases employing available solution thermodynamics and FLMTO quantum-mechanical calculations of compound stabilities identified the  $\text{Pd}_2\text{HfAl}$   $L2_1$  Heusler phase as the most promising first candidate in terms of stability and lattice parameter, supported by preliminary calculations using the FLAPW method. Quaternary alloys were studied to validate and refine phase relations. Measured tie-tetrahedra in the Nb-Pd-Hf-Al system directly established the composition limits of the desired BCC- $\text{Pd}_2\text{HfAl}$  two phase field, and a potentially useful BCC- $\text{Pd}_2\text{HfAl}$ -PdAl three-phase field, as reported in a recent publication [5]. The tie-tetrahedra in the Nb-Pd-Hf-Al system existing at 1200°C and the projection of the tetrahedra on the Pd-Hf-Al basal plane are shown in Figures 2 and 3 respectively.

Table I. Calculated properties for selected Heusler phases [3,4]

Compound	$a$ (calc), nm (at 0 K)	$a$ (expt), nm (at 298 K)	Lattice mismatch (w.r.t pure Nb at 298 K)	$-\Delta E$ (formation) (kJ/mol-atom)
$\text{Ni}_2\text{TiAl}$	0.587	0.5872, 0.5865	-11.1% to -11.05%	82.71
$\text{Ni}_2\text{VAl}$	0.578	0.633	-12.4% to -4.11%	62.36
$\text{Ni}_2\text{ZrAl}$	0.610	0.6123	-7.58% to -7.24%	80.35
$\text{Ni}_2\text{NbAl}$	0.600	0.5974	-9.5% to -9.09%	66.83
$\text{Ni}_2\text{HfAl}$	0.610	0.6081	-7.88% to -7.58%	91.51
$\text{Ni}_2\text{TaAl}$	0.595	0.5949	-9.88% to -9.87%	75.89
$\text{Pd}_2\text{HfAl}$	0.633	0.6367	-4.11% to -3.55%	77.69

<sup>1</sup>Numbers in parentheses in Figure 3 represent the phase Nb content in at. pct. measured by standard EDS (Energy Dispersive Spectroscopy) SEM analysis using Nb L-alpha Xrays, typically showing less than 1 at. pct. Nb. Recent analysis using Nb K-alpha Xrays however indicates the Nb contents may be as high as 10 at. pct., suggesting high L-alpha absorption, and further microanalysis conducted at a higher accelerating voltage is underway to resolve this apparent discrepancy.

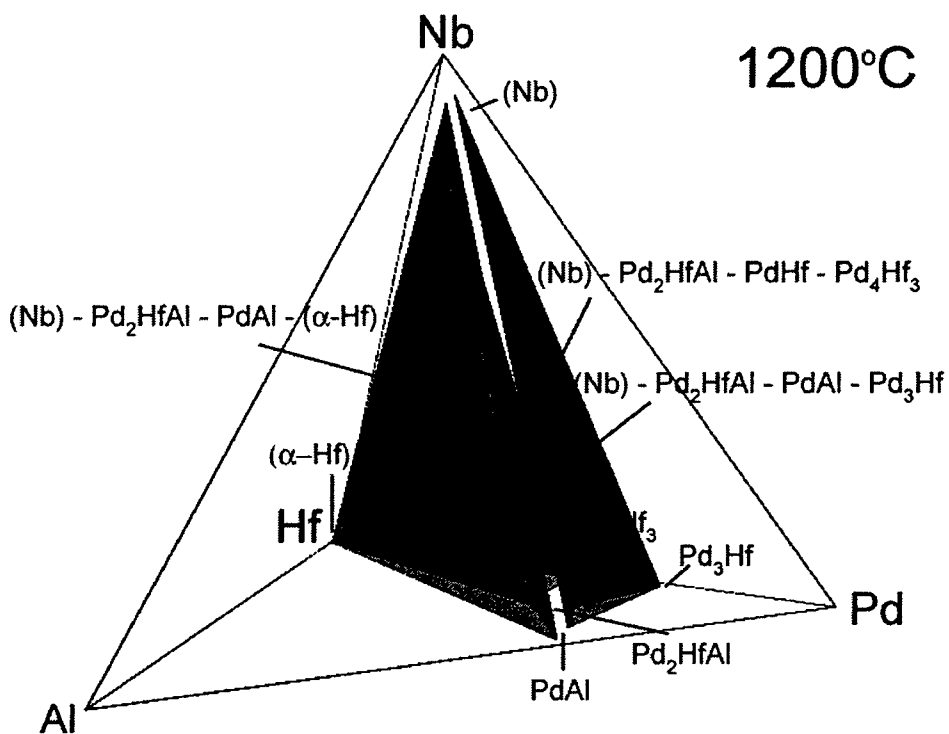


Figure 2. Tie-tetrahedra in the Nb-Pd-Hf-Al quaternary system at 1200°C.

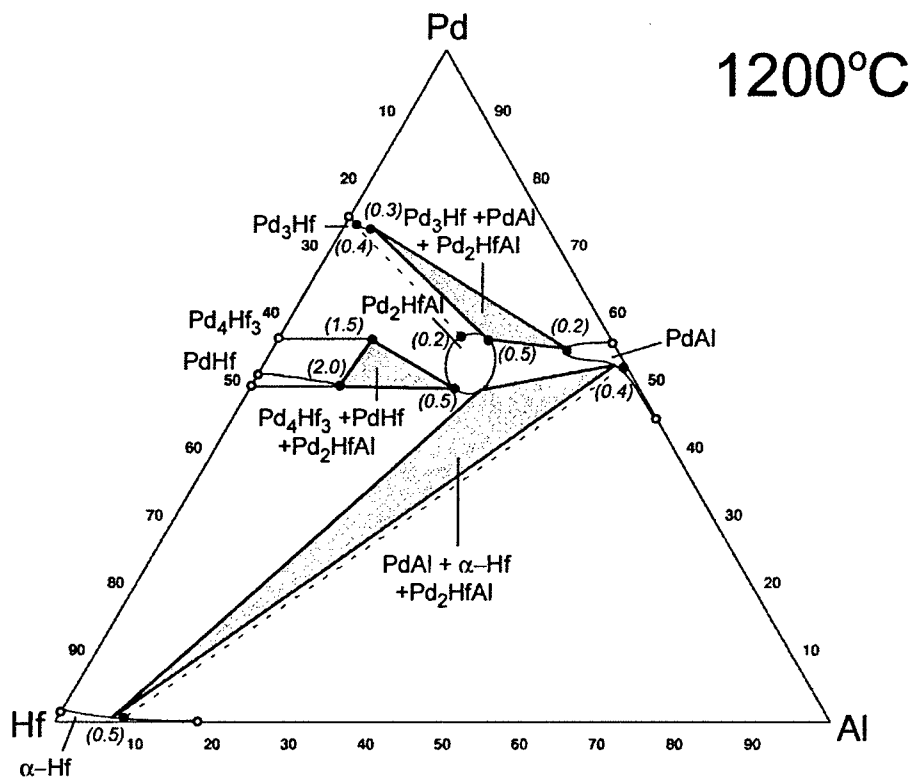


Figure 3. Projection of the Nb-Pd-Hf-Al tie-tetrahedra bases on the Pd-Hf-Al plane (1200°C).

A thorough reassessment of the solution thermodynamics of this system is underway integrating well chosen electronic calculations of compound formation energies employing both FLAPW all-electron and VASP pseudopotential methods. New procedures for efficiently integrating CALPHAD thermodynamic assessments with selective electronic-level total-energy calculations have been developed in collaboration with Prof. Mark Asta of Northwestern using a cluster expansion description of solid solutions. Our recently published assessment of the Nb-Hf system [6] has now been expanded to the Nb-Al and Hf-Al systems to describe the Nb-Hf-Al ternary system (Figure 4). Lattice parameter calculations are integrated into a molar volume database for control of interphase misfit. Efficient thermodynamic assessments combine calculated 0°K formation energies with measured compound melting points and phase boundaries to define entropic contributions.

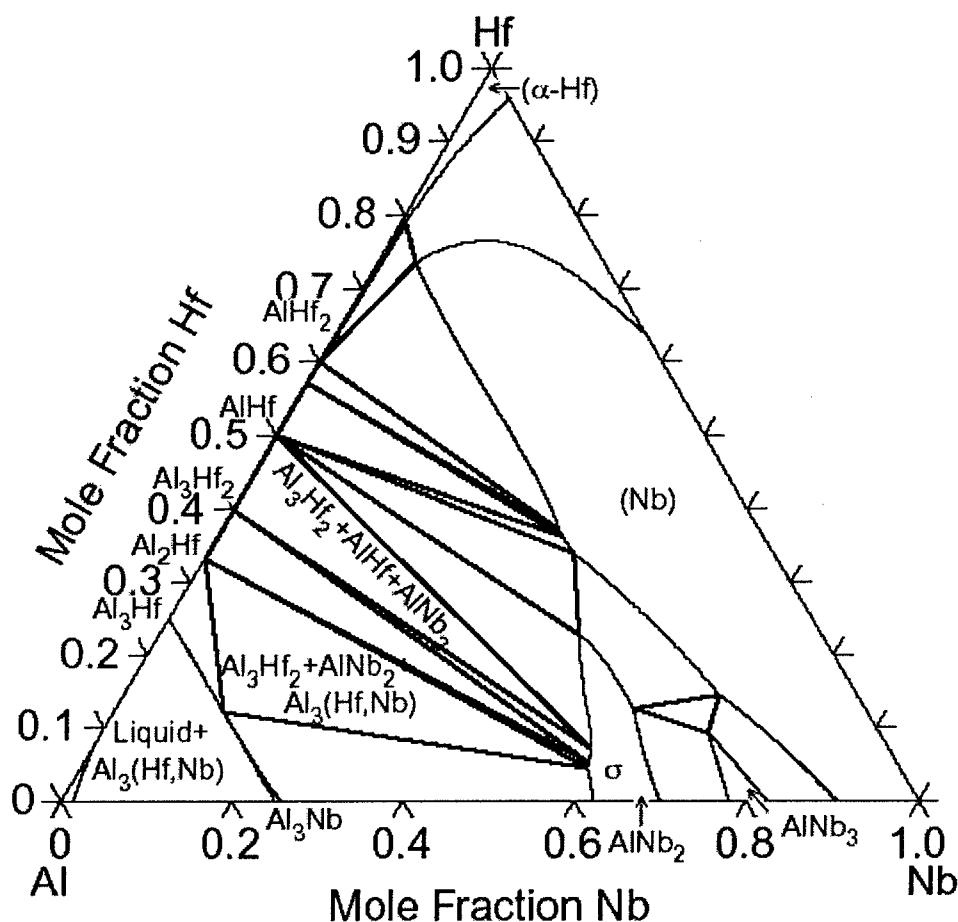


Figure 4. Calculated isothermal section of the Nb-Hf-Al system at 1300°C.

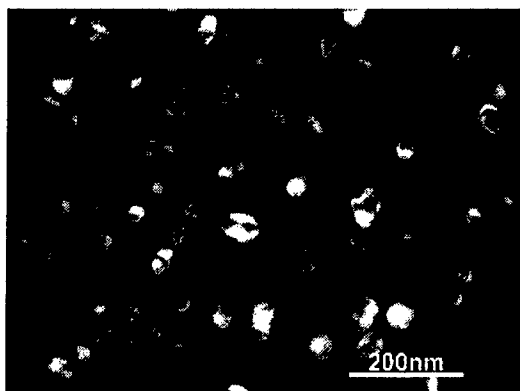
Based on the thermodynamics so far established, model alloys demonstrate desired fine dispersions of L2<sub>1</sub> Pd<sub>2</sub>HfAl and B2 PdAl in a Nb matrix as shown by the dark field TEM micrographs of Figure 5 taken using aluminide superlattice reflections [7]. The model alloys show a high microstructural stability at 1000°C compared to Ni-base alloys. Further TEM studies are underway to test for a novel octahedral morphology of coherent precipitates predicted for the unusual "inverse" elastic anisotropy of Nb alloys.

FLAPW calculations for the Heusler phase with partial substitution of Zr in the Hf sublattice predict slight improvement of both thermodynamic stability and lattice parameter for low misfit with Zr addition.

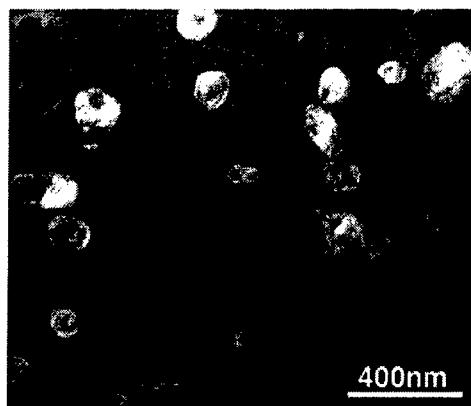
Based on relative stabilities of B2 binary compounds, partial substitution of Pt for Pd was next explored for further improvement. Figure 6 summarizes the predicted enthalpy of formation, enthalpy of mixing, and molar volume for both the Hf-Zr and Pd-Pt intermixing in the  $L2_1$ -structured  $(Pd,Pt)_2(Hf,Zr)Al$  Heusler phase. The curves represent best fits of the Redlich-Kister polynomials employed in our solution thermodynamic databases. Although Pt substitution strongly enhances thermodynamic stability and lattice expansion for reduced misfit, the  $L2_1$  Heusler phase treated here is no longer the ground state structure in the limit of the  $Pt_2(Hf,Zr)Al$  compositions. The predicted Hf-Zr intersolubility in  $Pd_2(Hf,Zr)Al$  has been confirmed by  $Pd_2HfAl$ - $Pd_2ZrAl$  diffusion couple experiments at  $1100^\circ C$  (Figure 7). A manuscript reporting these results is in preparation [8].

**(a) Prototype Nb-Al-Hf-Pd Alloy**  
 81.51Nb-9.34Pd-2.80Hf-6.34Al, at%;  
 As cast followed by  $1000^\circ C$  for 200 hrs

**(b) Prototype Nb-Al-Pd Alloy**  
 84Nb-8Pd-8Al (in at%)  
 As cast followed by  $1000^\circ C$  for 500 hrs



Heusler ( $Pd_2HfAl$ ) Precipitates  
 in a (Nb) Matrix



PdAl Precipitates in a (Nb)  
 Matrix

Figure 5. Dark-field TEM micrographs of  $Pd_2HfAl$  and PdAl dispersions in Nb alloys [7].

Toward optimization of matrix solution composition, electronic calculations also explore valency effects on interstitial O activity employing bond topological concepts [9]. Computed charge densities in the octahedral sites of BCC Nb and Mo account for an observed [10] dependence of O solubility on alloy electron/atom ( $e/a$ ) ratio. The predictions for alloying elements in BCC Nb are summarized in Figure 8 showing the trend holds until the  $e/a$  of Ru. Short-range order of B2 type is being investigated for the BCC Nb-based solid solution in order to promote 2nd neighbor bonding across the octahedral site as a more efficient means of increasing the site charge density. Incorporating O in both thermodynamic and atomic mobility databases, composition directions are predicted for reduced O solubility and enhanced Al/O diffusivity ratio. The mobility database is also augmented by electronic-level calculations of diffusion energetics with emphasis on prediction of slow-diffusing components for control of multicomponent coarsening resistance [11]. The predicted activation energy for self-diffusion in BCC Ta is in very good agreement with experiment, but is 15% low for the case of Nb. For dilute solution interdiffusivities in Nb alloys, we have employed a five-frequency model for correlation effects incorporating vacancy-solute interactions up to second nearest neighbors. Figure 9 summarizes measured and predicted diffusivities at  $1300^\circ C$  relative to the self-diffusivity of Nb. The predicted relative diffusivity of Mo is in good agreement with experiment. In our search for slow diffusers to enhance microstructural stability, we are very encouraged by the prediction that the activation energy for Re

diffusion is 50% higher than that of Mo, giving a Re diffusivity as low as W, the slowest diffuser yet measured. In support of the prediction, a Nb/Re diffusion couple has shown no measurable intermixing at 1100°C, and higher temperatures are next being investigated.

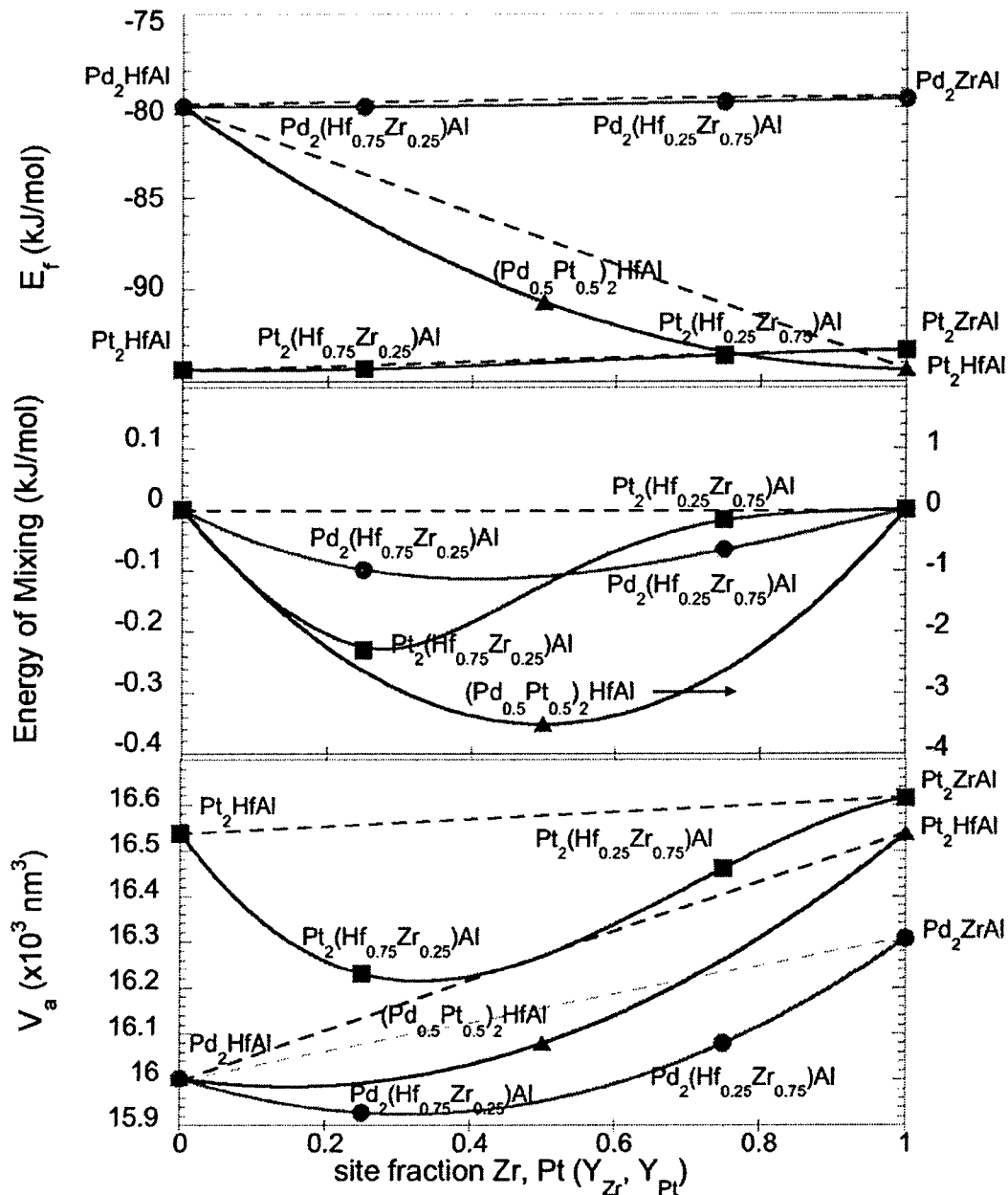


Figure 6. FLAPW calculations of heat of formation, heat of mixing, and molar volume in the  $(\text{Pd,Pt})_2(\text{Hf,Zr})\text{Al } L2_1$  phase.

Preliminary oxidation studies on both model alloys and Heusler intermetallics demonstrate continuous scale formation involving varying combinations of  $\text{Al}_2\text{O}_3$  and  $\text{HfO}_2$ , but do not yet demonstrate desired recession rates. Employing the models and databases thus far developed integrated via the THERMOCALC thermodynamic and DICTRA diffusion kinetic codes, a team of students in an undergraduate Materials Design class at Northwestern has performed the theoretical design of oxidation

resistant Nb alloys with a combination of Pd<sub>2</sub>HfAl and PdAl phases dispersed in a multicomponent BCC Nb-based matrix. With thermodynamically compatible additions of Mo, W and Ru in the matrix, the theoretical designs satisfy the Wagner criterion for Al<sub>2</sub>O<sub>3</sub> passivation at 1300°C reducing O solubility by 10<sup>-2</sup>, reducing O diffusivity by 10<sup>-1</sup> and enhancing Al diffusivity by 10<sup>3</sup>. Their project report [12] was submitted to the TMS-AIME Undergraduate Design Competition, winning 1st Prize for 2004. Prototype alloy validation is underway. Further designs to be evaluated in the next year employ multicomponent oxide scales for more efficient passivation.

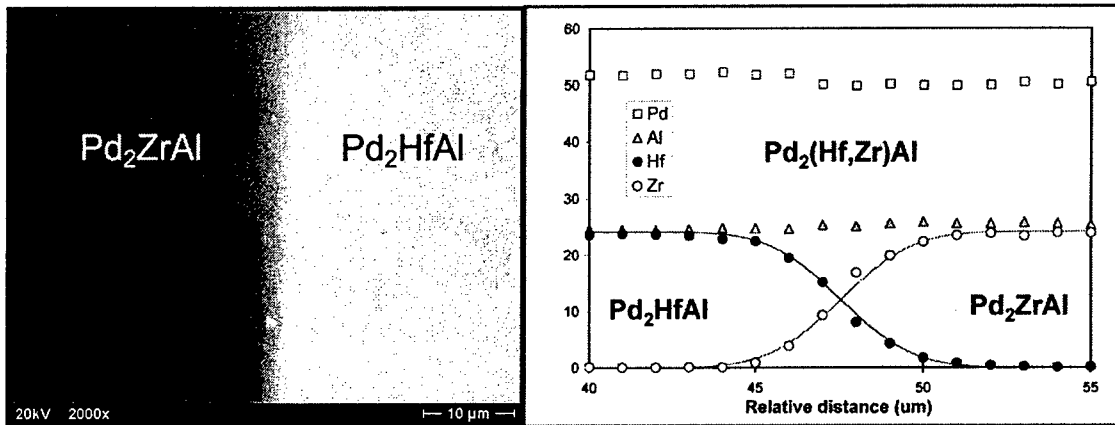


Figure 7. (a) BSE image of cross section of the Pd<sub>2</sub>ZrAl/Pd<sub>2</sub>HfAl diffusion couple; (b) Concentration profile obtained from (a) by EPMA [8].

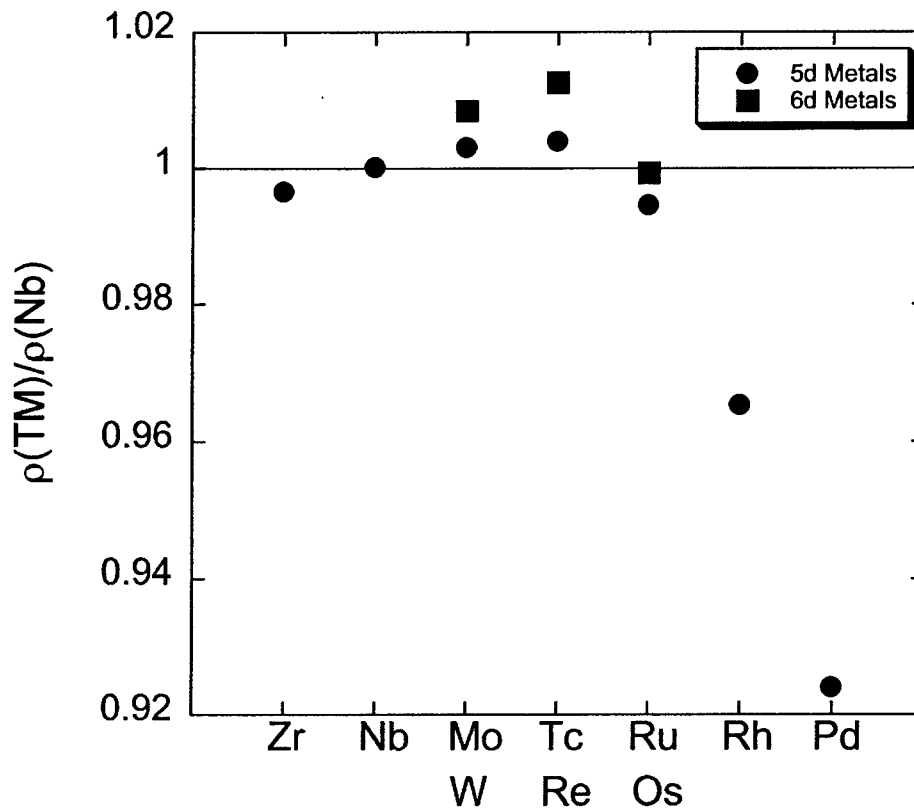


Figure 8. Computed charge density in BCC octahedral sites adjacent to solute atoms in Nb solid solution, scaled to pure Nb case [9].

## Relative diffusion of elements in Niobium at 1573 K

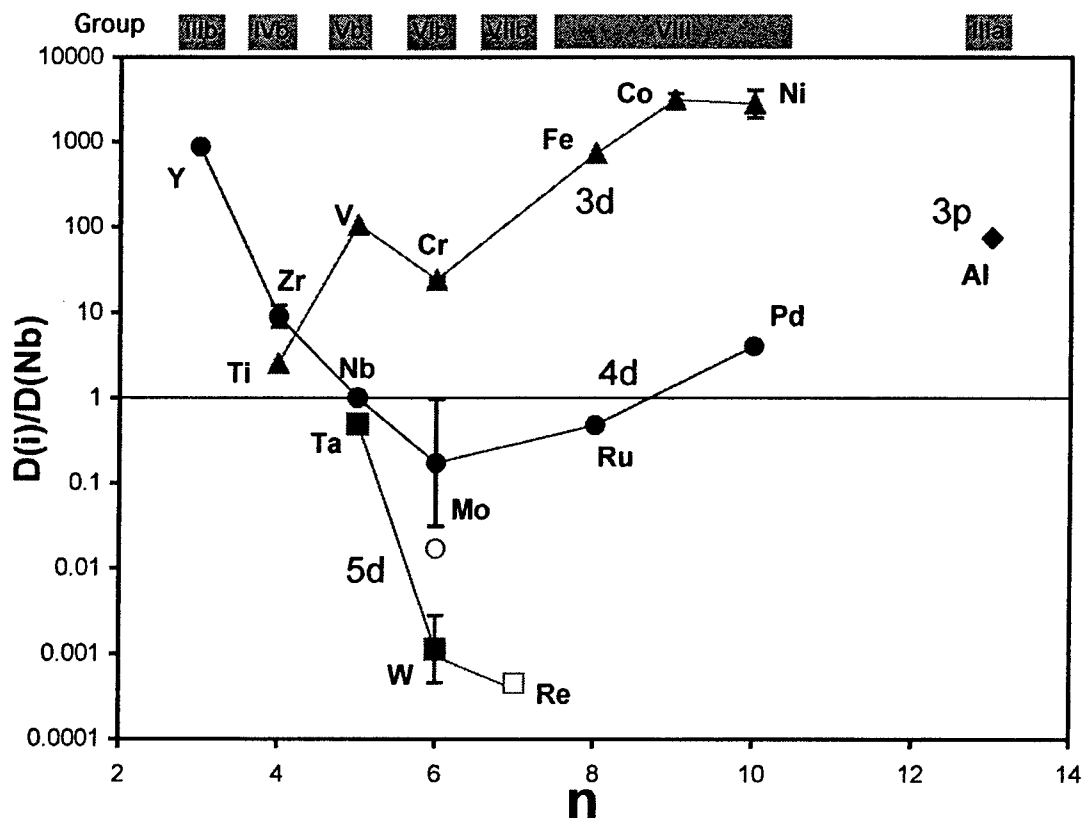


Figure 9. Measured and predicted dilute interdiffusivities in Nb at 1300°C, normalized to Nb self-diffusivity [11].

### Conclusions

Efficient integration of quantum mechanical 0°K formation energy calculations with selective measurement of high temperature phase relations allows accelerated development of thermodynamic databases for computational materials design, of particular importance for novel systems such as Nb base alloys where experimental phase diagram data is limited. An important byproduct of the quantum mechanical calculations is the rapid development of molar volume databases supporting control of interphase misfit. Quantitative charge density calculations can also provide guidelines for rapid assessment of interstitial solution thermodynamics governing oxygen solubility behavior. Computational quantum mechanics can also provide useful estimates of substitutional component diffusivities, identifying candidate slow diffusers to enhance microstructural stability at high temperatures.

The integration of these capabilities in the computational design of Nb base alloys exploiting precipitation strengthening by coarsening resistant controlled-misfit coherent multicomponent aluminide phases offers a high potential for combining oxidation resistance and creep strength for application at 1300°C and above.

### Acknowledgments/Disclaimer

This work was sponsored by the Air Force Office of Scientific Research, USAF, under grant number F49620-01-1-0529, with additional support from Reference Metals Company, Inc., and computer time grants from San Diego Supercomputing Center and ERDC. Researchers contributing to this project

include post-doctoral associate M. Kim of Northwestern, graduate students R. Bishop, D. Bryan and A. Misra of Northwestern and S. Kim of U. Wisconsin. The views and conclusions contained herein are those of the authors and should not be interpreted as necessarily representing the official policies or endorsements, either expressed or implied, of the Air Force Office of Scientific Research or the U.S. Government.

### References

1. G.B. Olson, "Computational Design of Hierarchically Structured Materials," *Science*, 277 (5300) (1997), 1237-1242.
2. C. Wagner, "Reaction Types with the Oxidation of Alloys," *Z. Elektrochemie*, 63 (1959), 772-782.
3. W. Lin and A.J. Freeman, *Physical Review B*, 45 (1992), 61-68.
4. M. Kim and A.J. Freeman, Northwestern University, Evanston, IL, unpublished research, 2002.
5. A. Misra, R. Bishop, G. Ghosh and G.B. Olson, "Phase Relations in Prototype Nb-Pd-Hf-Al Alloys," *Metallurgical and Materials Transactions A*, 34A (2003), 1771-1781.
6. G. Ghosh, A. van de Walle, M. Asta and G. B. Olson, "Phase Stability of the Hf-Nb System: From First-Principles to CALPHAD," *CALPHAD*, 26 (4) (2002), 491-511.
7. G. Ghosh and G.B. Olson, Northwestern University, Evanston, IL, unpublished research, 2003.
8. M. Kim, A.J. Freeman, S. Kim, J. Perepezko and G.B. Olson, "Phase Stability of the Multicomponent Intermetallic L<sub>2</sub> Heusler Phase (Pd,Pt)<sub>2</sub>(Hf,Zr)Al," manuscript in preparation.
9. M. Eberhart, Colorado School of Mines, Golden, CO, unpublished research, 2003.
10. R.T. Bryant, "The Solubility of Oxygen in Transition Metal Alloys," *Journal of Less-Common Metals*, 4 (1962) 62-68.
11. C. Woodward, Northwestern University, Evanston, IL, unpublished research, 2003.
12. E. Altinoglu, J. Bolos and N. Colligan, "Noburnium: Oxidation Resistant Nb Superalloy," Northwestern University, MSc 390 Materials Design project report (May 2003), submitted to TMS-AIME Undergraduate Design Competition.

## Final Report for MEANS I

John H. Perepezko and Sungtae Kim  
University of Wisconsin-Madison

**CURRENT STUDY**

Currently, the Ni-based superalloys are used at temperatures close to their operating limits ( $< 1100\text{ }^{\circ}\text{C}$ ) that are greater than 90% of their melting temperatures. Increases in the operating temperature play a key role in advancing in high performance turbine engines because use temperatures limit the efficiency of the turbo engines. In this regard, the Nb-based alloys system has been selected as a high-temperature application because niobium has a high melting temperature ( $2468\text{ }^{\circ}\text{C}$ ) and low density ( $8.6 \times 10^3\text{ kg/m}^3$ ). However, niobium has a poor oxidation resistance. In order to address this issue it is necessary to develop an alloy design that yields a protective oxide scale in the event of an exposure to high temperature environment. Moreover, to minimize high temperature creep, the alloy design includes a strengthening with a fine precipitate of a secondary ordered phase. In the alloy design the  $L2_1$  Heusler ( $X_2YZ$ ) phase has been selected, with aluminum in the Z sites, because the strengthening phase in a given Nb bcc matrix should have a bcc-type crystal structure.

The bcc-type  $\text{Pd}_2\text{XAl}$  ( $X = \text{Hf, Zr}$ ) Heusler phases are attractive since they represent a second phase that exhibits the least lattice parameter discrepancy with the bcc-Nb matrix. Moreover, the formation of stable  $\text{HfO}_2$ ,  $\text{ZrO}_2$ , and  $\text{Al}_2\text{O}_3$  oxides is expected to play a key role in protecting the multiphase design against oxidation. Nevertheless, the physical property database for the  $\text{Pd}_2\text{XAl}$  Heusler phases is limited. In order to address the high temperature stability of the Nb-based alloys system, it is necessary to examine the high temperature oxidation resistance of the  $\text{Pd}_2\text{XAl}$  Heusler phase and the phase stability between the  $\text{Pd}_2\text{XAl}$  Heusler phase and the bcc-Nb matrix. Therefore, we have facilitated the identification of the key features of the multicomponent phase stability and the oxidation kinetics. The oxidation resistance and stability database for the monolithic  $\text{Pd}_2\text{XAl}$  Heusler phases provide critical input data for the computational design of advanced high temperature materials.

**1.  $\text{Pd}_2(\text{Hf,Zr})\text{Al}$  Heusler Phases as a second phase**

Previously, from a thermodynamic calculation the melting temperature of  $\text{Pd}_2\text{HfAl}$  was estimated at about  $3000\text{ }^{\circ}\text{C}$  [bis01]. Based on the binary phase diagram of the Hf-Zr system [asm92], Hf and Zr are completely miscible to form the ( $\alpha\text{Hf}$ ,  $\alpha\text{Zr}$ ) and ( $\beta\text{Hf}$ ,  $\beta\text{Zr}$ ) solid solution phases, as shown in figure 1. Complete mixing between Hf and Zr leads to predicting a continuous compositional homogeneity region between  $\text{Pd}_2\text{HfAl}$  and  $\text{Pd}_2\text{ZrAl}$  by substitution of Hf to Zr and of Zr to Hf. To confirm the continuity between  $\text{Pd}_2\text{HfAl}$  and  $\text{Pd}_2\text{ZrAl}$ , an  $\text{Pd}_2\text{ZrAl}/\text{Pd}_2\text{HfAl}$  diffusion couple was annealed at  $1100\text{ }^{\circ}\text{C}$  for 50 hours. A back-scattered electron (BSE) image of the cross section of the annealed  $\text{Pd}_2\text{ZrAl}/\text{Pd}_2\text{HfAl}$  diffusion couple is shown in figure 2(a), in which the diffusion reaction zone between  $\text{Pd}_2\text{ZrAl}$  and  $\text{Pd}_2\text{HfAl}$  exhibits a contrast gradient with distance. The continuous contrast change in the diffusion reaction zone indicates the probable continuity of the compositional homogeneity between  $\text{Pd}_2\text{ZrAl}$  and  $\text{Pd}_2\text{HfAl}$ . Concentration profiles (figure 2(b)) obtained from line scanning across

the diffusion reaction zone by an electron probe microanalysis (EPMA) show slight changes in the Pd and Al concentrations between Pd<sub>2</sub>ZrAl and Pd<sub>2</sub>HfAl, which originally came from difference between nominal composition and fabricated alloy composition of a Heusler phase. The concentrations of Hf and Zr change symmetrically over distance in the diffusion reaction zone. This corroborates that Hf and Zr atoms substitute each other on the X sublattice sites in a Pd<sub>2</sub>XAl Heusler phase while Pd and Al atoms remain on their own lattice sites. Consequently, complete mixing of Hf and Zr atoms forms a solution phase Pd<sub>2</sub>(Hf,Zr)Al. The diffusional behavior of Hf and Zr in the Pd<sub>2</sub>ZrAl/Pd<sub>2</sub>HfAl diffusion couple can be regarded as a Hf-Zr pseudo-binary interdiffusion in Pd<sub>2</sub>(Hf,Zr)Al. Based on diffusion analysis in a binary system, the interdiffusion coefficient for the Hf-Zr pseudo-binary system in Pd<sub>2</sub>(Hf,Zr)Al was estimated as  $7.9 \times 10^{-18} \text{ m}^2/\text{s}$  at 1100 °C.

According to the preliminary pseudo-binary phase diagram calculation of the Nb-Pd<sub>2</sub>HfAl system [bis01], the liquidus temperature is  $1670 \pm 40$  °C for Nb-30Pd-15Hf-15Al (all compositions are given as at%) and  $1780 \pm 40$  °C for Nb-20Pd-10Hf-10Al. The pseudo-binary phase diagram also shows that Pd<sub>2</sub>HfAl melts congruently above 3000 °C. However, the as-cast Pd<sub>2</sub>HfAl and Pd<sub>2</sub>ZrAl alloys were observed to melt during annealing at 1500 °C, which is far below the calculated melting temperature of Pd<sub>2</sub>HfAl. A big discrepancy between the melting temperature from the preliminary pseudo-binary phase diagram of the Nb-Pd<sub>2</sub>HfAl system and 1500 °C at which the as-cast alloys melted, consequently, requires a re-evaluation of the melting temperature of the Pd<sub>2</sub>XAl Heusler phase. In order to identify safe temperatures for annealing the Pd<sub>2</sub>ZrAl/Pd<sub>2</sub>HfAl diffusion couple, as-cast alloys were heated up with a rate of 40.0 °C/min from 200 °C to 1410 °C and cooled down with the same rate by a Differential Thermal Analyzer (DTA, Perkin Elmer). The DTA analysis results are shown in figure 3, in which the onset melting temperature of the as-cast Pd<sub>2</sub>HfAl and Pd<sub>2</sub>ZrAl Heusler phases are estimated at 1440 and 1350 °C. For the as-cast Pd<sub>2</sub>HfAl alloy, there exists a small peak at about 1250 °C during the cooling process. Identification of the small peak has not yet been completed to determine whether the peak belongs to a solid-state transformation or to solidification of the remaining liquid phase. Continuous homogeneity between Pd<sub>2</sub>HfAl and Pd<sub>2</sub>ZrAl requires assessing the onset melting temperatures of the Pd<sub>2</sub>(Hf,Zr)Al phase. Figure 4 shows the assessed onset melting temperatures of the Pd<sub>2</sub>(Hf<sub>x</sub>Zr<sub>1-x</sub>)Al where  $0 \leq x \leq 1$ . The as-cast Pd<sub>2</sub>(Hf<sub>x</sub>Zr<sub>1-x</sub>)Al initiates melting at a temperature between 1350 and 1440 °C.

## 2. Oxidation Behavior of the bcc-type Heusler Phases and B2 Phase

A key element of the high temperature Nb alloy design is based upon the use of bcc-related phases in a multiphase microstructure to achieve elevated temperature strengthening and oxidation resistance. To examine oxidation resistance at high temperature, the selected bcc-type Pd<sub>2</sub>HfAl (L2<sub>1</sub> Heusler phase), Pd<sub>2</sub>ZrAl (L2<sub>1</sub> Heusler phase) and PdAl (B2 CsCl crystal structure) alloys were oxidized at 1100 and 1300 °C for 25 hours in air. A cross section SEM-BSE image of the oxidized Pd<sub>2</sub>HfAl alloy at 1100 °C for 25 hours (figure 5(a)) shows that three distinct layers developed during high temperature oxidation: (i) an outermost dense and hard layer consisting of Al<sub>2</sub>O<sub>3</sub>, HfO<sub>2</sub> and PdO<sub>2</sub>, (ii) a mixed layer of oxides (HfO<sub>2</sub> and Al<sub>2</sub>O<sub>3</sub>) and intermediate phase (PdAl), and (iii) a mixture of PdAl and Pd<sub>3</sub>Hf. Composition measurements by an EPMA identified the existence of oxygen in the (i) and (ii) layers, resulting in an oxygen penetration depth about 50 – 60 μm out of about 85 – 95 μm for the total thickness of three layers. The PdO<sub>2</sub> phase was observed in XRD spectra collected from the oxidized Pd<sub>2</sub>HfAl at 1100 °C. However, it is reported that PdO<sub>2</sub> decomposes to PdO at 200 °C, and PdO decomposes

to Pd at 750 °C [Web]. In this regard, existence of PdO<sub>2</sub> in the oxidized Pd<sub>2</sub>HfAl could be interpreted that Pd oxides form during cooling of the sample in air, or that the HfO<sub>2</sub> and Al<sub>2</sub>O<sub>3</sub> oxides in the (i) layer limit the decomposition of PdO<sub>2</sub>.

The Pd<sub>2</sub>HfAl oxidized at 1300 °C for 25 hours developed the (i), (ii) and (iii) layers with a total thickness of about 12-14 μm (figure 5(b)). The oxygen penetration depth at 1300 °C was measured at about 7 - 8 μm. The thickness of three layers formed by the oxidation reaction decreases at higher temperature, indicating an enhancement of oxidation protection with increasing temperature. Figure 6 shows the weight change of Pd<sub>2</sub>HfAl as a function of oxidation time that was obtained from an oxidation experiment at 1300 °C by a Thermogravimetric Analyzer (TGA). The TGA analysis indicates the passive oxidation behavior of Pd<sub>2</sub>HfAl at 1300 °C because of continuous weight gain. This implies that the inward (from surface to inside) diffusion of oxygen dominates the oxidation kinetics rather than the outward (from inside to surface) diffusion of Pd, Hf and Al. Consequently, oxides form at the interfaces between the (i) and (ii) layers, and the (ii) and (iii) layers during the oxidation reaction.

A microstructural morphology of three distinct layers developed by oxidation reaction can be analyzed to establish an oxidation reaction pathway, (PdO<sub>2</sub>+HfO<sub>2</sub>+Al<sub>2</sub>O<sub>3</sub>) / (HfO<sub>2</sub>+Al<sub>2</sub>O<sub>3</sub>+PdAl) / (HfO<sub>2</sub>+PdAl) / PdAl / (PdAl+Pd<sub>3</sub>Hf) / (PdAl +Pd<sub>3</sub>Hf+Pd<sub>2</sub>HfAl) / Pd<sub>2</sub>HfAl, as shown in figure 5(c). Identification of the three-phase equilibrium among PdAl, Pd<sub>3</sub>Hf and Pd<sub>2</sub>HfAl in figure 5(c) indicates the stability of the PdAl-Pd<sub>3</sub>Hf, Pd<sub>3</sub>Hf-Pd<sub>2</sub>HfAl and PdAl-Pd<sub>2</sub>HfAl two-phase equilibria. Observation of the two-phase equilibria and a three-phase equilibrium coincides with the projected Nb-Pd-Hf-Al tie-tetrahedra bases on the Pd-Hf-Al plane at 1200 °C [mis03]. To determine the phase boundary compositions of PdAl, Pd<sub>3</sub>Hf and Pd<sub>2</sub>HfAl in their three-phase equilibrium, an EPMA line scanning from the Pd<sub>3</sub>Hf-PdAl two-phase equilibrium region to the Pd<sub>2</sub>HfAl phase region was performed to obtain the Pd, Hf and Al concentration profiles (figure 5(d)). The phase boundary composition of Pd<sub>2</sub>HfAl in the Pd<sub>3</sub>Hf-PdAl-Pd<sub>2</sub>HfAl three-phase equilibrium that was estimated from the Pd<sub>3</sub>Hf/Pd<sub>2</sub>HfAl interface in figure 5(d) exhibits a deviation from the stoichiometric composition, indicating an extension of the compositional homogeneity of Pd<sub>2</sub>HfAl. According to the concentration profiles in figure 5(d), the composition deviation reveals that the Pd<sub>2</sub>HfAl phase is Pd-rich with a composition of Pd<sub>50+2y</sub>Hf<sub>25-y</sub>Al<sub>25-y</sub> (0 ≤ y ≤ 2.5 at%) over a distance of about 30 μm. The formation of the Pd-rich Pd<sub>2</sub>HfAl near the Pd<sub>3</sub>Hf-PdAl-Pd<sub>2</sub>HfAl three-phase equilibrium region (or near the interface between the Pd<sub>2</sub>HfAl phase and the PdAl-Pd<sub>3</sub>Hf two-phase region) appears to result from Al and Hf transport to three distinct layers that is related to formation of Al<sub>2</sub>O<sub>3</sub> and HfO<sub>2</sub> oxides.

A cross section SEM image of the oxidized Pd<sub>2</sub>ZrAl alloy at 1100 °C for 25 hours is shown in figure 7, where five distinguishable layers formed during high temperature oxidation: (i) a layer consisting of Al<sub>2</sub>O<sub>3</sub>, ZrO<sub>2</sub> and PdO<sub>2</sub>, (ii) a ZrO<sub>2</sub> oxide layer, (iii) a layer of ZrO<sub>2</sub> and ρ (Pd<sub>75</sub>Al<sub>25</sub>), (iv) mixture of Al<sub>2</sub>O<sub>3</sub> and ZrO<sub>2</sub>, and (v) another layer consisting of ZrO<sub>2</sub> and ρ. Cracks were observed to run through the (ii) layer, resulting in peeling of the oxide layer scale. An EPMA analysis and the SEM image (figure 7) show an oxygen penetration depth of about 700 μm for the 25-hour oxidation. Fast and deep oxygen penetration appears to result in complete consumption of the base Pd<sub>2</sub>ZrAl phase because composition measurements by an EPMA identified that the base alloy below the (v) layer exhibited a composition of ρ (Pd<sub>75</sub>Al<sub>25</sub>). This indicates that Zr substitution on the X sublattice sites in a Pd<sub>2</sub>XAl Heusler phase degrades the oxidation resistance.

The XRD spectra collected from the oxidized PdAl alloys also exhibit the presence of PdO<sub>2</sub>. Cross section SEM-BSE images (figure 8) of the oxidized PdAl alloys at 1100 and 1300

°C show that a dense  $\text{Al}_2\text{O}_3$  oxide layer covers the surface of the PdAl phase and contains Pd. This indicates that the dense  $\text{Al}_2\text{O}_3$  oxide layer may include  $\text{PdO}_2$  that is observed in the XRD analysis. Once again, the existence of  $\text{PdO}_2$  in the oxidized PdAl alloys could be interpreted that Pd oxides form during cooling of the sample in air, or that  $\text{Al}_2\text{O}_3$  limits the decomposition of Pd oxides. The measured  $\text{Al}_2\text{O}_3$  oxide layer thickness is nearly the same at about 2  $\mu\text{m}$  at 1100 °C and 1300 °C. Consequently, it may be concluded that a thin (1 – 3  $\mu\text{m}$ ) oxide layer mixed with  $\text{Al}_2\text{O}_3$  and  $\text{PdO}_2$  protects the PdAl phase at 1100 and 1300 °C, indicating enhancement of the oxidation protection at increasing temperature.

### 3. Phase Stability and Diffusion Kinetics between Nb and a bcc-type second phase

To examine the high-temperature stability between pure Nb and a  $\text{Pd}_2\text{XAl}$  Heusler phase, diffusion couple experiments were performed. The Nb/ $\text{Pd}_2\text{ZrAl}$ , Nb/ $\text{Pd}_2\text{HfAl}$  and Nb/PdAl diffusion couples were annealed at 1100 °C under a Ti-gettered Ar atmosphere. Figure 9(a) shows the SEM-BSE image of the cross section of the Nb/ $\text{Pd}_2\text{HfAl}$  diffusion couple annealed at 1100 °C for 50 hours. The annealing process generated several intermediate phases between Nb and  $\text{Pd}_2\text{HfAl}$ . Composition measurements by an EPMA determined that the intermediate phases are Hf(ss), PdAl, and  $\text{Pd}_3\text{Hf}$ . Figure 9(a) shows that the Hf(ss) phase includes a fine-scale second phase that is not identified because of its size. During isothermal annealing, the Nb/ $\text{Pd}_2\text{HfAl}$  diffusion couple developed a diffusion reaction path Nb / Hf(ss) / Hf(ss)+PdAl / PdAl / PdAl+ $\text{Pd}_3\text{Hf}$  / PdAl+ $\text{Pd}_3\text{Hf}$ + $\text{Pd}_2\text{HfAl}$  /  $\text{Pd}_2\text{HfAl}$  at 1100 °C, as shown in figure 9(b). The reaction product layers exhibit a total thickness of about 50  $\mu\text{m}$ .

Figure 10(a) shows a SEM-BSE image of the cross section of the Nb/ $\text{Pd}_2\text{ZrAl}$  diffusion couple annealed at 1100 °C for 50 hours. The annealing process generated several intermediate phases between Nb and  $\text{Pd}_2\text{ZrAl}$ . The EPMA measurements determined that the intermediate phases are Zr(ss) and PdAl, where the Zr(ss) phase may have some porosity. During isothermal annealing, the Nb/ $\text{Pd}_2\text{ZrAl}$  diffusion couple developed a diffusion reaction path Nb / Zr(ss) / Zr(ss)+PdAl / Zr(ss)+PdAl+ $\text{Pd}_2\text{ZrAl}$  /  $\text{Pd}_2\text{ZrAl}$  at 1100 °C, as shown in figure 10(b). The reaction product layers exhibit a total thickness of about 60  $\mu\text{m}$ . In fact, the Hf-Zr binary phase diagram shows formation of the ( $\alpha\text{Hf}$ ,  $\alpha\text{Zr}$ ) and ( $\beta\text{Hf}$ ,  $\beta\text{Zr}$ ) complete solid solution phases, indicating the similarity of Hf and Zr, and their mutual complete solubility. Consequently, the diffusion kinetics in the Nb/ $\text{Pd}_2\text{HfAl}$  and Nb/ $\text{Pd}_2\text{ZrAl}$  couples was expected to be similar. However, during isothermal annealing, the Nb/ $\text{Pd}_2\text{HfAl}$  diffusion couple developed Hf(ss), PdAl and  $\text{Pd}_3\text{Hf}$  while the Nb/ $\text{Pd}_2\text{ZrAl}$  diffusion couple developed Zr(ss) and PdAl. This established two distinct diffusion pathways of the Nb/ $\text{Pd}_2\text{HfAl}$  (figure 9(b)) and Nb/ $\text{Pd}_2\text{ZrAl}$  (figure 10(b)) couples.

Figure 11(a) shows the SEM-BSE image of a cross section of the Nb/PdAl diffusion couple annealed at 1100 °C for 150 hours. Sluggish Nb, Pd and Al atom movements resulted in a negligible concentration change (figure 11(b)), and no product phase was observed between Nb and PdAl. This result suggests that a Nb-PdAl two-phase equilibrium may exist so that the phase combination of Nb and PdAl at 1100 °C would not be degraded by the formation of byproduct phases. In 1987, Kiseleva calculated the stability of Heusler phases using the relation of the atomic dimension of components and electron concentration as well as thermodynamic and electron properties of components. He predicted stable formation of the  $\text{Pd}_2\text{NbAl}$  Heusler phase. If  $\text{Pd}_2\text{NbAl}$  is in equilibrium with both (Nb) and PdAl, a ternary equilibrium among (Nb), PdAl and  $\text{Pd}_2\text{NbAl}$  would occur (figure 12). This allows for a multiphase design of  $\text{BCC}(\text{Nb}) + \text{B2}(\text{PdAl}) + \text{L}_{21}(\text{Pd}_2\text{NbAl})$ , where  $\text{L}_{21}$  and B2 belong to the bcc-based crystal structure. Figure

13 shows a SEM-BSE image of as-cast Pd-25Nb-25Al (at% in unit) alloy, in which an EPMA analysis identified the co-existence of (Nb), PdAl and Pd<sub>2</sub>NbAl.

To develop an effective database for the diffusion behavior in Nb binary alloys, diffusion experiments have been conducted on interdiffusion in the Nb/Re and Nb/Ru couples. For the diffusion treatment at 1100 °C, the Nb/Re diffusion couple was annealed for 200 hours under a Ti-gettered Ar atmosphere. For the heat treatment at 1600 °C that is about 300 °C higher than the intended use temperature of the Niobium alloys, the Nb/Re diffusion couple was annealed for 100 hours under a high vacuum atmosphere of  $7 \times 10^{-7}$  Torr. The cross section of the 1100 °C diffusion couple is shown in figure 14(a), in which contrast of each end member pure element is discrete at the interface. The Nb and Re concentrations were measured across the interface by an EPMA with a 20kV acceleration voltage and 20 nA current. Based on the Nb and Re concentration profiles, Nb and Re atom movements are sluggish and develop a narrow diffusion zone with a width of about 3  $\mu\text{m}$  along the interface. The profiles elucidate that the diffusion process does not form the  $\chi$  intermediate phase that exhibits the homogeneity region ranging from 63.5 – 87 at%Re. In other words, Nb atoms diffuse in the (Re) solid solution and Re atoms in the (Nb) solid solution. An error function regression fit on experimentally measured concentration profile data, was used to estimate the interdiffusion coefficient of (Nb) at  $\tilde{D} = 2.4 \times 10^{-19} \text{ m}^2/\text{s}$ . Because the displacements of the Kirkendall voids (black dots on the interface in figure 14(a)) can be negligible, the estimated interdiffusion coefficient may approximate the intrinsic diffusion coefficient.

The cross section of the Nb/Re diffusion couple annealed at 1600 °C is shown in figure 14(b), in which the  $\chi$  intermediate phase forms between Nb and Re. An EPMA analysis measured the Nb and Re concentration profiles as a function of distance. According to the profiles, Nb and Re atom movements develop a diffusion reaction zone of about 40 – 45  $\mu\text{m}$ . The (Nb) solution phase exhibits the Re solubility of about 44 at%Re. The compositional homogeneity range of the  $\chi$  phase extends from 64.3 at%Re to 86.1 at%Re. This is consistent with the published phase diagram of the Nb-Re system, where the Re solubility of (Nb) is 44.3 at% Re and the homogeneity region of  $\chi$  ranges from 63 – 87 at%Re. By fitting an error function, based on an assumption of constant diffusivity, the estimated interdiffusion coefficients of (Nb) and  $\chi$  are  $2.6 \times 10^{-16} \text{ m}^2/\text{s}$  and  $6.0 \times 10^{-18} \text{ m}^2/\text{s}$ , respectively. A plot of diffusion coefficients versus the reciprocal temperature is shown in figure 15, in which the interdiffusion coefficients of (Nb) are compared with the Nb self-diffusivities. At 1600 °C the Nb self-diffusivity is faster than the (Nb) interdiffusion coefficient while at 1100 °C the Nb self-diffusivity is slower than the (Nb) interdiffusion coefficient. This means that at 1100 °C the chemical potential gradient for directive atom movements is a dominant driving force rather than the thermal energy for random jumps is.

The Nb/Ru diffusion couple that was annealed at 1200 °C for 200 hours developed two distinct product layers (figure 16(a)); two layers are labeled as layer 1 and layer 2. The Nb and Ru concentration profiles (figure 16(b)) obtained by an EPMA line scanning on the Nb/Ru diffusion couple determined the compositional homogeneity ranges of two layers that are not comparable to a binary Nb-Ru phase diagram (figure 16(c)) in reference **asm92**. This requires a re-assessment of the detailed phase stability in the Nb-Ru binary system. Based on the concentration profiles, as shown in figure 16(b), the interdiffusion coefficient of (Nb) was estimated as  $5.0 \times 10^{-18} \text{ m}^2/\text{s}$ , which can be compared to the Nb self-diffusivity of  $4.3 \times 10^{-19} \text{ m}^2/\text{s}$  at 1200 °C.

## SUMMARY OF ACCOMPLISHMENTS

As a selected second phase in the Nb-based alloy design for improving the oxidation resistance and for minimizing high temperature creep, the Pd<sub>2</sub>XAl (X = Hf, Zr) Heusler phases have been examined. Complete miscibility between Hf and Zr yields a solution phase Pd<sub>2</sub>(Hf,Zr)Al, where Hf and Zr atoms substitute each other on the X sublattice sites in a Pd<sub>2</sub>XAl Heusler phase while Pd and Al atoms remain on their own sublattice sites. The DTA analysis reveals that the as cast Pd<sub>2</sub>(Hf<sub>x</sub>Zr<sub>1-x</sub>)Al where  $0 \leq x \leq 1$  initiates melting at a temperature between 1350 – 1440 °C, which is far below the thermodynamic calculation that Pd<sub>2</sub>HfAl melts congruently above 3000 °C.

To examine oxidation resistance, the bcc-type L2<sub>1</sub> Pd<sub>2</sub>XAl Heusler phases and B2 PdAl phase were oxidized at 1100 and 1300 °C in air. Three distinct layers developed during oxidation of Pd<sub>2</sub>HfAl. The Pd<sub>2</sub>HfAl phase below three distinct layers exhibits a Pd-rich composition of Pd<sub>50+2y</sub>Hf<sub>25-y</sub>Al<sub>25-y</sub> ( $0 \leq y \leq 2.5$  at%) over a distance of about 30 μm. The TGA analysis indicates the passive oxidation behavior of Pd<sub>2</sub>HfAl at 1300 °C because of weight gain. From an analysis of the kinetics it is concluded that the inward diffusion of oxygen dominates the oxidation kinetics. During oxidation of Pd<sub>2</sub>ZrAl fast and deep oxygen penetration appeared to result in complete consumption of the base Pd<sub>2</sub>ZrAl, indicating that Zr substitution on the X sublattice sites in a Pd<sub>2</sub>XAl Heusler phase degrades the oxidation resistance. In the oxidized PdAl alloys it was observed that a dense Al<sub>2</sub>O<sub>3</sub> oxide layer covers the surface of PdAl and contains Pd. Measurements of Al<sub>2</sub>O<sub>3</sub> oxide layer thickness at 1100 and 1300 °C indicate enhancement of the oxidation protection at increasing temperature.

Diffusion couple experiments have examined the high-temperature phase stability and diffusion kinetics between pure Nb and a bcc-type second phase in the Nb-based alloy design. The Nb/Pd<sub>2</sub>HfAl diffusion couple that was annealed at 1100 °C for 50 hours developed the intermediate phases Hf(ss), PdAl and Pd<sub>3</sub>Hf with a total reaction product layers thickness of about 50 μm. The Nb/Pd<sub>2</sub>ZrAl diffusion couple that was annealed at 1100 °C for 50 hours developed the intermediate phases Zr(ss) and PdAl with a total reaction product layers thickness of about 60 μm. Annealing the Nb/PdAl diffusion couple at 1100 °C for 150 hours did not generate any reaction product, indicating a probable Nb-PdAl two-phase equilibrium. This predicts a multiphase design of BCC(Nb) + B2(PdAl) + L2<sub>1</sub>(Pd<sub>2</sub>NbAl), provided that the Pd<sub>2</sub>NbAl Heusler phase exists as a stable phase and is in equilibrium with both (Nb) and PdAl. From the Nb/Re diffusion couple experiments the (Nb) interdiffusion coefficient was estimated as  $2.4 \times 10^{-19}$  m<sup>2</sup>/sec at 1100 °C and  $2.6 \times 10^{-16}$  m<sup>2</sup>/sec at 1600 °C. At 1600 °C the Nb self-diffusivity is faster than the (Nb) interdiffusion coefficient while at 1100 °C the Nb self-diffusivity is slower than the (Nb) interdiffusion coefficient. The Nb/Ru diffusion couple that was annealed at 1200 °C for 200 hours developed two distinct product layers. An EPMA analysis shows that the measured compositional homogeneity ranges of two layers are not comparable to the published Nb-Ru binary phase diagram.

## FUTURE DIRECTIONS

From the initial observations it is evident that the PdAl phase plays a major role in controlling the oxidation response. The PdAl intermediate phase was observed in the multiple-layer structures that were formed on the Pd<sub>2</sub>HfAl and Pd<sub>2</sub>ZrAl phases by oxidation. Since PdAl forms an Al<sub>2</sub>O<sub>3</sub> oxide layer by oxidation, a Pd-rich PdAl is expected to develop below the Al<sub>2</sub>O<sub>3</sub> oxide layer. In fact, the Al<sub>2</sub>O<sub>3</sub> oxide layer formed by oxidation reaction at 1300 °C is thinner

than the  $\text{Al}_2\text{O}_3$  oxide layer formed at 1100 °C, indicating the enhancement of oxidation protection with increasing temperature. Moreover, the crystal structures of B2 PdAl and a  $\text{L}_{21}$  Heusler phase ( $\text{Pd}_2\text{HfAl}$ ,  $\text{Pd}_2\text{ZrAl}$ , etc.) indicate that small additions of Hf or Zr into PdAl may substitute for Al. In this regard, the oxidation behavior could change with addition of Hf or Zr into PdAl and indicate another role for the Hf/Zr ratio in controlling the microstructure. Again, a similar behavior can be expected for PtAl and the substitution of Y for Hf or Zr.

In order to assess oxidation behavior, the PdAl design, in which Pd and Al compositions change continuously with distance, will be subject to heat treatment in air. Al-rich PdAl is expected to be less oxidation resistant behavior than Pd-rich PdAl, provided that PdAl is assumed to exhibit the similar diffusional behavior of NiAl. In the Al-rich PdAl, diffusion of Al atom movements may slow down as the composition below the  $\text{Al}_2\text{O}_3$  oxide layer reaches stoichiometry. This may increase the oxygen penetration depth and the thickness of the oxide layer. In other words, the oxide layer structure may be expected to change with composition of PdAl.

A number of diffusion couple experiments involving Nb/PdAl, Nb/Re and Nb/Ru pairings should be performed at various temperatures to assess the diffusivities as well as phase stabilities that determine the equilibrium microstructure. Since the standard diffusion couple experiment gives information about phase stability such as a tie line and diffusion kinetic properties only on the diffusion pathway, multiple standard diffusion couple explorations between two phases are necessary. For rapid assessments of phase stability and diffusion kinetics, diffusion couples and diffusion multiples can be employed where the diffusion multiple is an assembly of three or more different alloys. Continued experiments on diffusion couples made by assembling two pure metals such as Nb-Re, Nb-Ru and other pairings can demonstrate the diffusion behavior and contribute essential information for the stable phase boundary database. A diffusion multiple can be constructed by adding another member such as Nb to the  $\text{Pd}_2\text{HfAl}/\text{Pd}_2\text{ZrAl}$  couple either before or after  $\text{Pd}_2\text{HfAl}$  and  $\text{Pd}_2\text{ZrAl}$  undergo diffusion reaction. With the addition of the third member the diffusion multiple can be used to probe within multicomponent phase space and identify the multiple tie lines that are necessary for a phase stability analysis. Moreover, based upon the diffusion multiple exploration, specific intermediate phase diffusion couples can be designed to allow for an accurate evaluation of the component diffusivities.

A key objective will be to identify means to control the diffusion pathway. For instance, due to the similarity of Hf and Zr and their mutual solubility, the diffusion kinetics in the Nb/ $\text{Pd}_2\text{HfAl}$  and Nb/ $\text{Pd}_2\text{ZrAl}$  couples is expected to be similar. However, following an anneal at 1100 °C, Hf(ss),  $\text{Pd}_3\text{Hf}$  and PdAl developed in the Nb/ $\text{Pd}_2\text{HfAl}$  diffusion couple while only Zr(ss) and PdAl developed in the Nb/ $\text{Pd}_2\text{ZrAl}$  diffusion couple. This corroborates that the diffusion behavior between Nb and the  $\text{Pd}_2(\text{Hf,Zr})\text{Al}$  phase changes dramatically at certain composition ratio of Hf to Zr. Moreover, the change in the diffusion kinetics between Nb and  $\text{Pd}_2(\text{Hf,Zr})\text{Al}$  indicates that the microstructure of the Nb-Pd-(Hf,Zr)-Al system can be controlled by the Hf/Zr composition ratio. Consequently, the Nb/ $\text{Pd}_2(\text{Hf,Zr})\text{Al}$  diffusion multiple experiments with a variation of the Hf/Zr composition ratio are of special interest.

## **REFERENCES**

- [asm96] ASM International, ASM Handbook: vol. 3 Alloy Phase Diagrams, ASM International, Ohio, 1992, pp. 2.244, pp. 2.305.
- [bis01] R. R. Bishop, *Ph.D. thesis*, Northwestern University, Evanston, Illinois, 2001.
- [kis87] N. N. Kiseleva, *Izvestiya Akademii Nauk SSSR. Metallurgy*, 2, 213 (1987).

- [mis03] A. Misra, R. Bishop, G. Ghosh and G. B. Olson, *Metall. Mater. Trans. A*, 34A[9], 1771 (2003).
- [mis02] A. Misra, G. Ghosh and G.B. Olson, *Materials Technology Laboratory 5<sup>th</sup> Annual Meeting* (March 25-26, 2002), Evanston, IL (2002).
- [shu72] A.K. Shurin and V.V. Pet'kov, *Russ. Metall.*, 2, 122-144 (1972)
- [Web] <http://www.webelements.com>

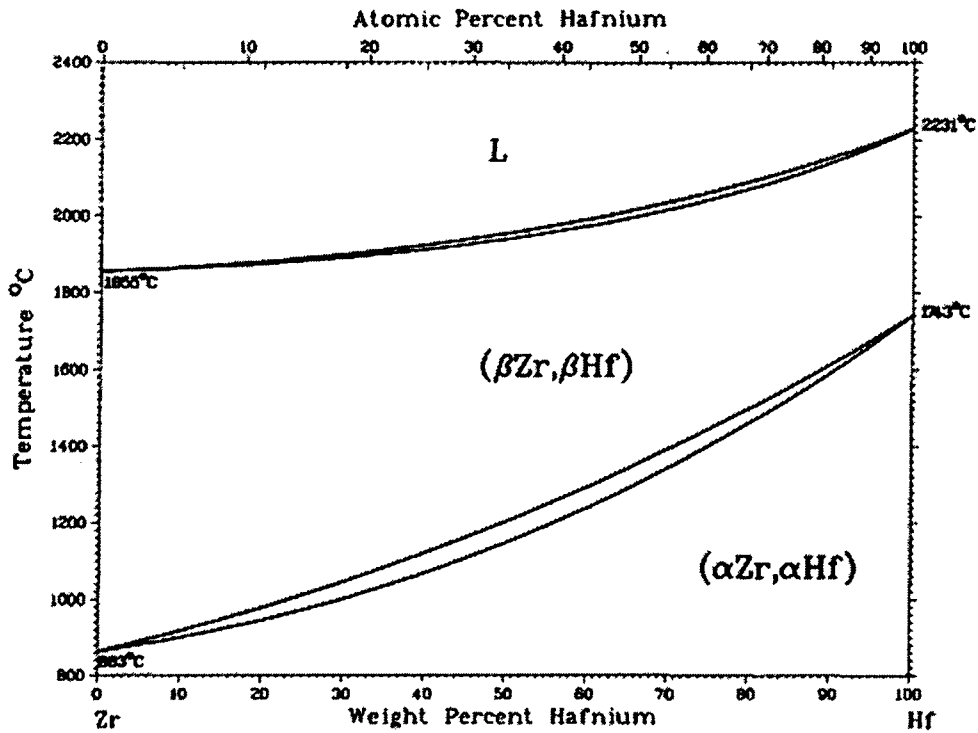


Figure 1. Zr-Hf binary phase diagram [asm]

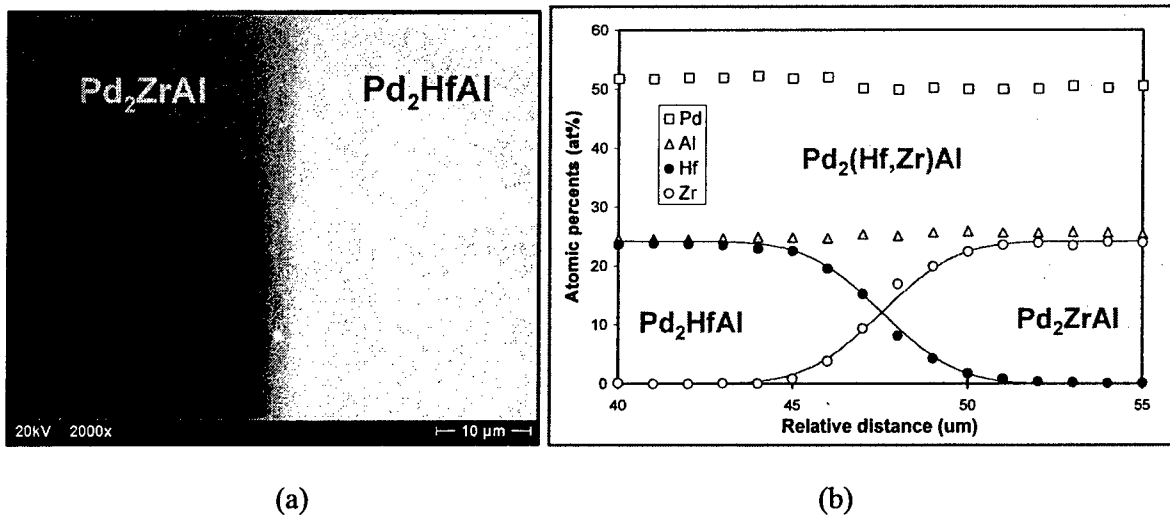


Figure 2. (a) SEM BSE image of the cross-section of the Pd<sub>2</sub>HfAl/Pd<sub>2</sub>ZrAl diffusion couple annealed at 1100 °C for 50 hours and (b) concentration profiles of Pd, Hf, Zr and Al obtained from the diffusion couple shown in (a).

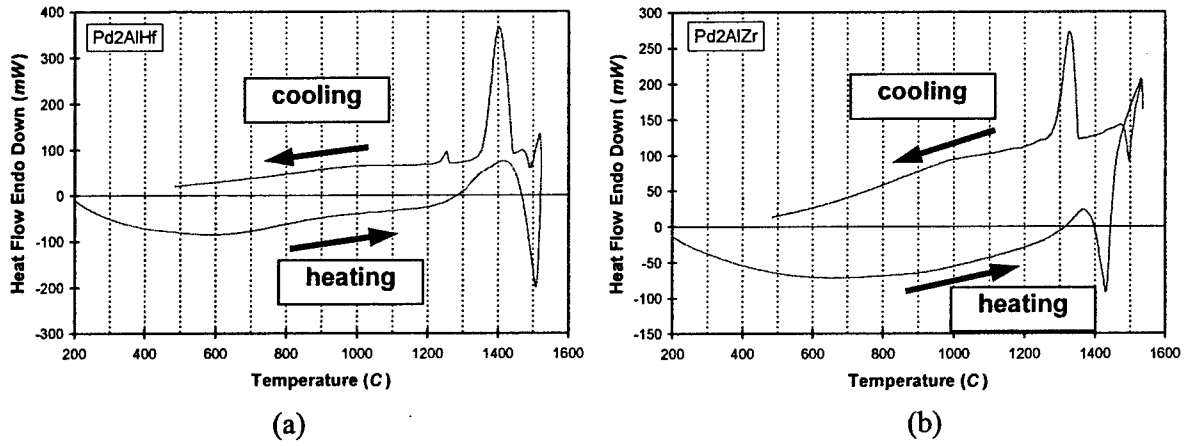


Figure 3. DTA curves of (a) as-cast Pd<sub>2</sub>HfAl and (b) as-cast Pd<sub>2</sub>ZrAl with a rate of 40.0 °C/min

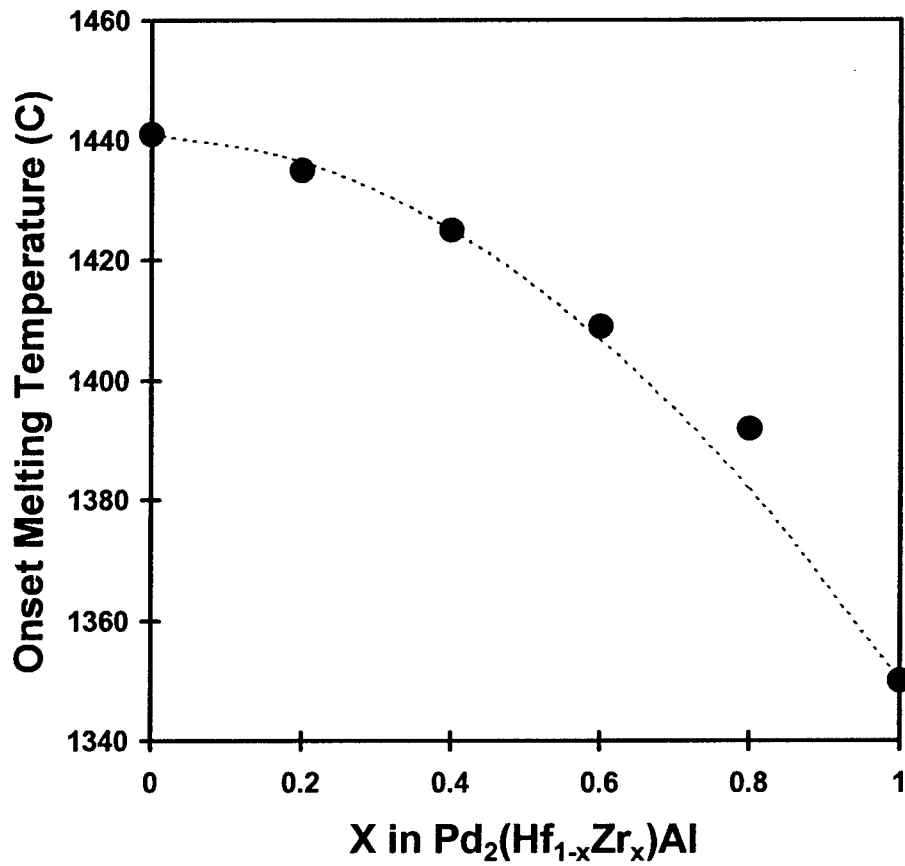
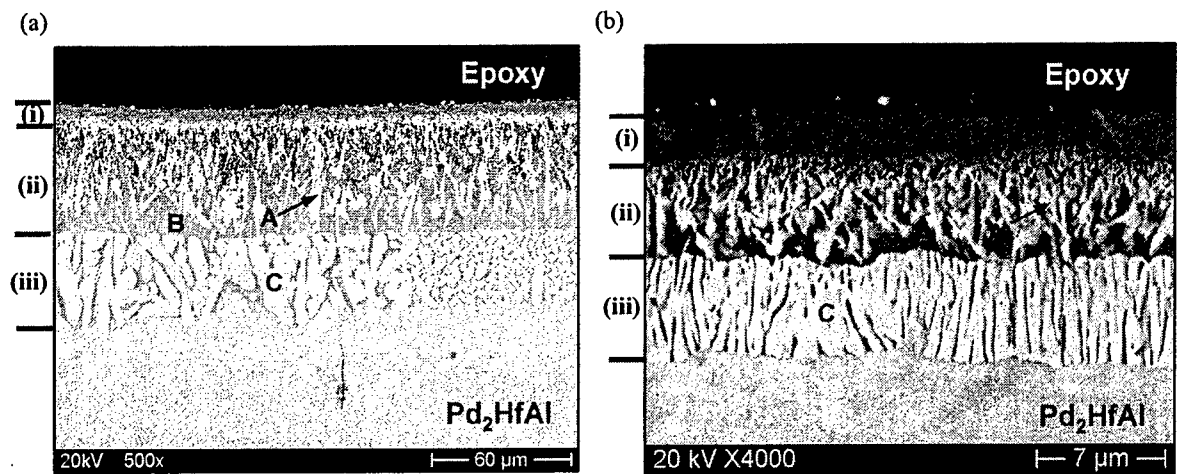


Figure 4. Onset melting temperature of Pd<sub>2</sub>(Hf<sub>1-x</sub>Zr<sub>x</sub>)Al, where 0 ≤ x ≤ 1.



- (i). Dense and hard layer ( $\text{Al}_2\text{O}_3 + \text{HfO}_2 + \text{PdO}_2$ )
- (ii).  $\text{A}(\text{HfO}_2) + \text{B}(\text{PdAl}) + \text{Black phase}(\text{Al}_2\text{O}_3)$
- (iii).  $\text{B}(\text{PdAl}) + \text{C}(\text{Pd}_3\text{Hf})$

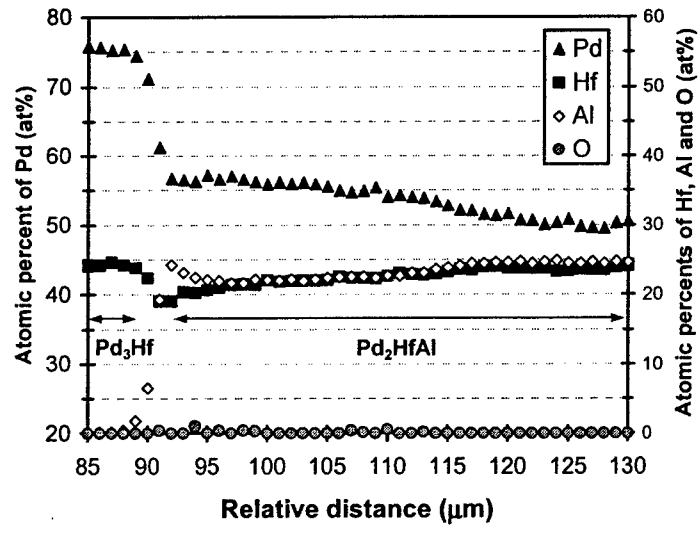
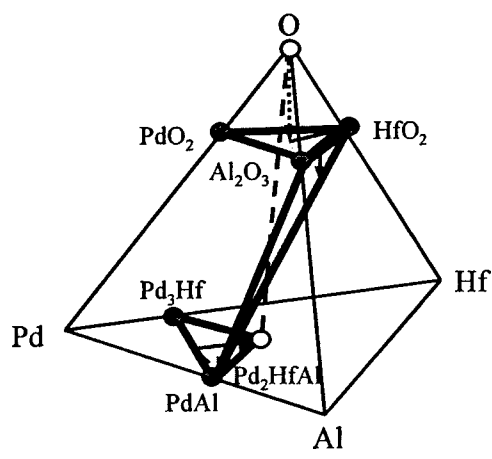


Figure 5. Cross section SEM-BSE images of the oxidized  $\text{Pd}_2\text{HfAl}$  alloys at (a) 1100 °C and (b) 1300 °C, showing three distinct layers: the (i) layer consists of  $\text{Al}_2\text{O}_3$ ,  $\text{HfO}_2$  and  $\text{PdO}_2$ , the (ii) layer consists of  $\text{HfO}_2$ ,  $\text{PdAl}$  and  $\text{Al}_2\text{O}_3$  (black phase), and the (iii) layer consists of  $\text{PdAl}$  and  $\text{Pd}_3\text{Hf}$ . (c) Schematic oxidation reaction pathway and (d) concentration profiles of Pd, Hf, Al and O measured over  $\text{Pd}_3\text{Hf}$ - $\text{PdAl}$  two-phase region and  $\text{Pd}_2\text{HfAl}$  region.

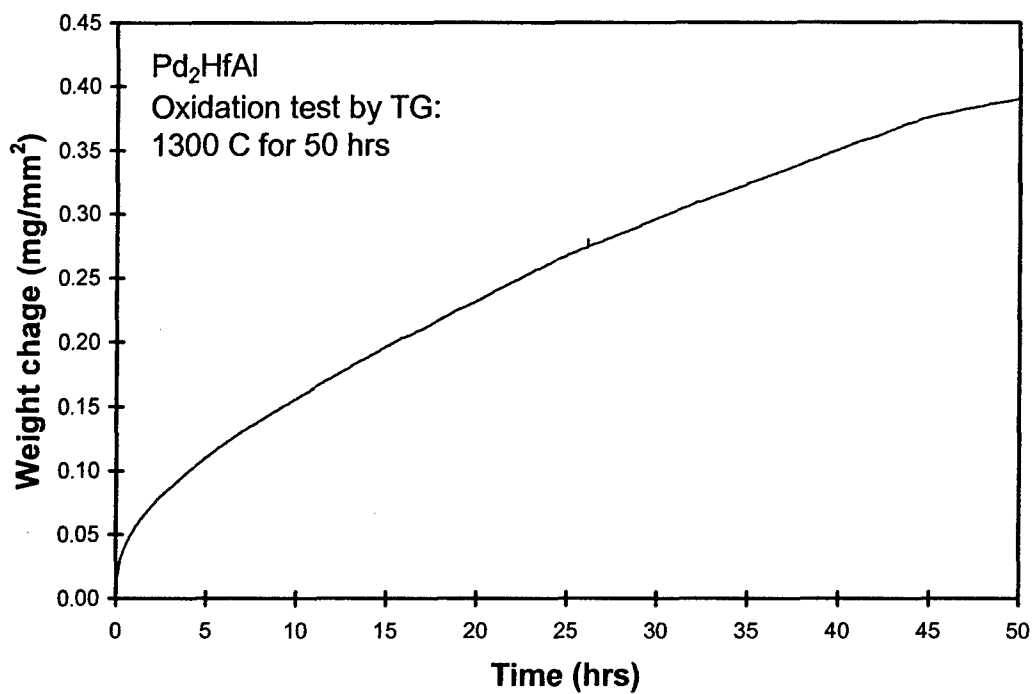


Figure 6. Plot of weight change of Pd<sub>2</sub>HfAl versus oxidation time, obtained from oxidation experiment at 1300 °C by the TGA.

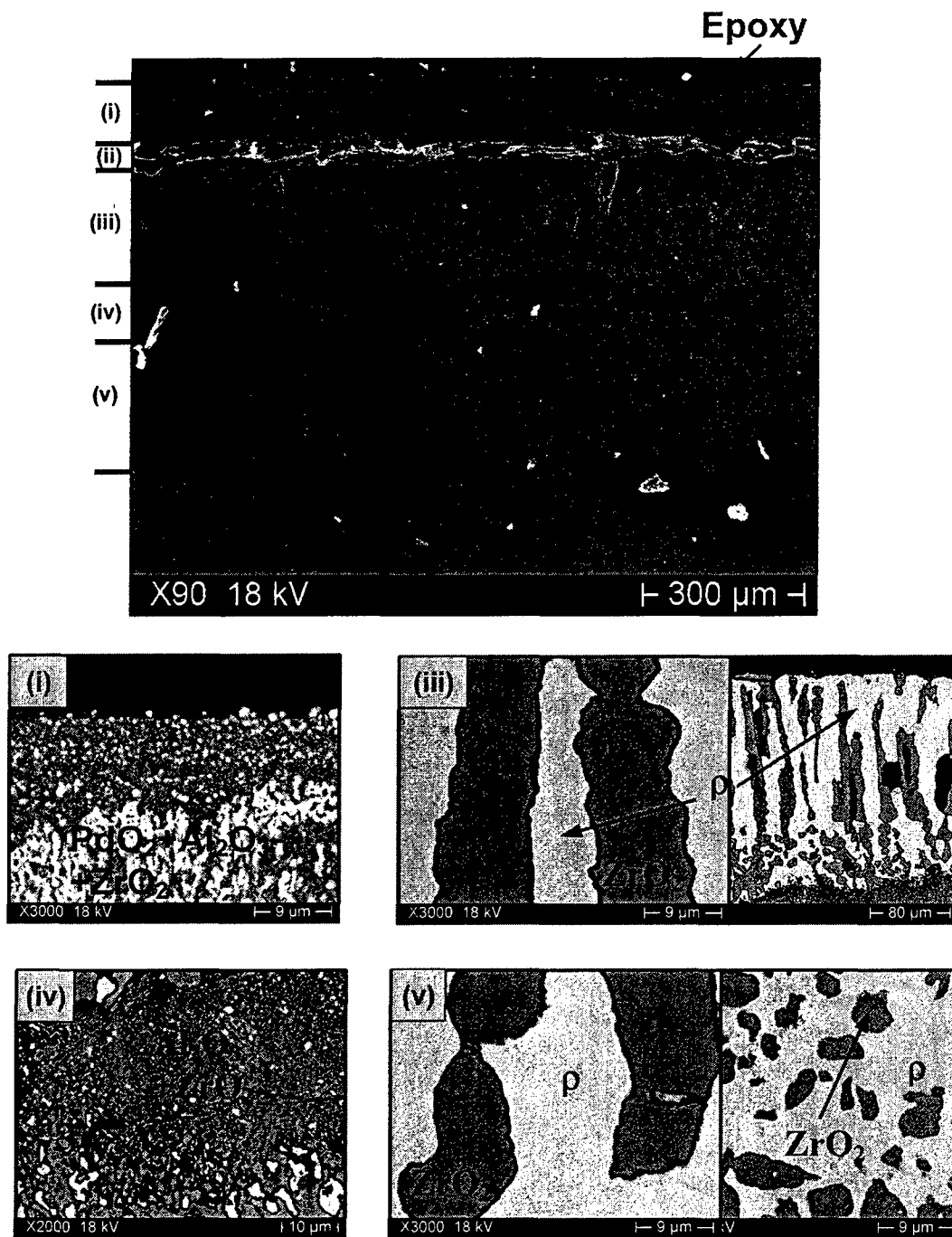


Figure 7. SEM-SE image of oxidized Pd<sub>2</sub>ZrAl alloy at 1100 °C for 25 hours, showing five distinct layers: the (i) layer consists of PdO<sub>2</sub>, Al<sub>2</sub>O<sub>3</sub> and ZrO<sub>2</sub>, the (ii) layer is a ZrO<sub>2</sub> oxide layer, the (iii) layer consists of ZrO<sub>2</sub> and ρ (Pd<sub>75</sub>Al<sub>25</sub>), the (iv) layer consists of Al<sub>2</sub>O<sub>3</sub> and ZrO<sub>2</sub>, and the (v) layer consists of ZrO<sub>2</sub> and ρ.

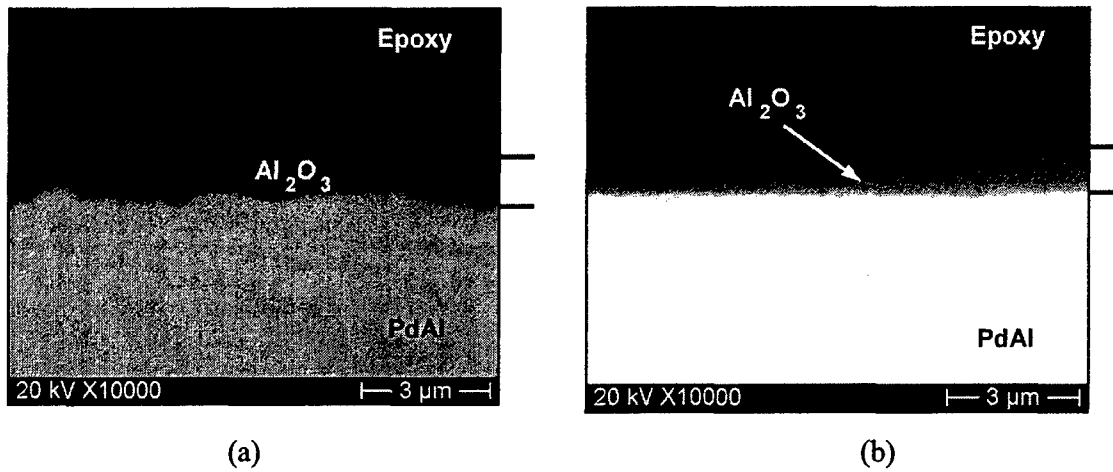


Figure 8. Cross section SEM-BSE images of the oxidized PdAl alloys at (a) 1100 °C and (b) 1300 °C for 25 hours.

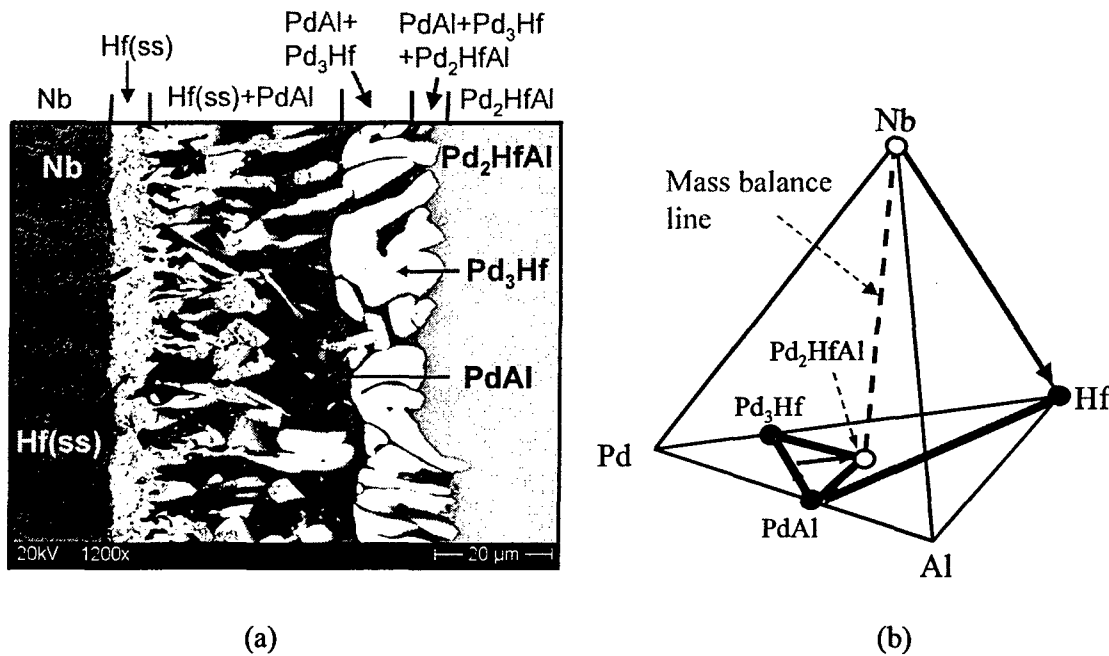


Figure 9. (a) SEM BSE image of the cross-section of the Nb/Pd<sub>2</sub>HfAl diffusion couple annealed at 1100 °C for 50 hours and (b) schematic diffusion pathway.

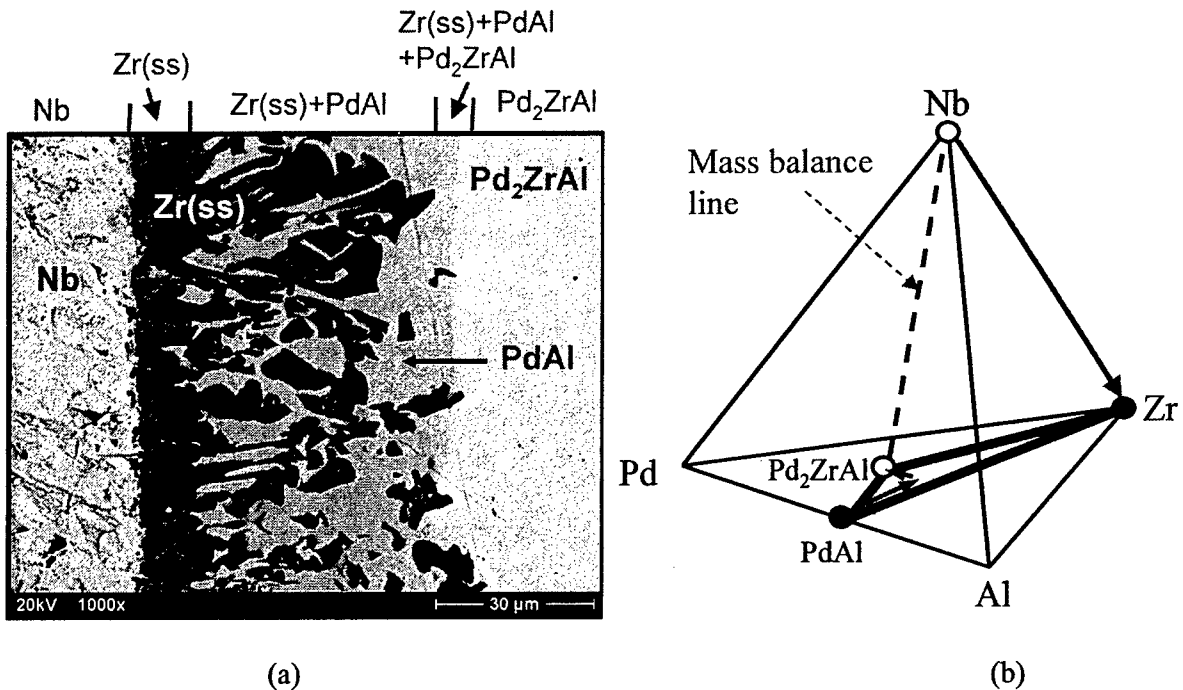


Figure 10. (a) SEM BSE image of the cross-section of the Nb/Pd<sub>2</sub>ZrAl diffusion couple annealed at 1100 °C for 50 hours and (b) schematic diffusion pathway.

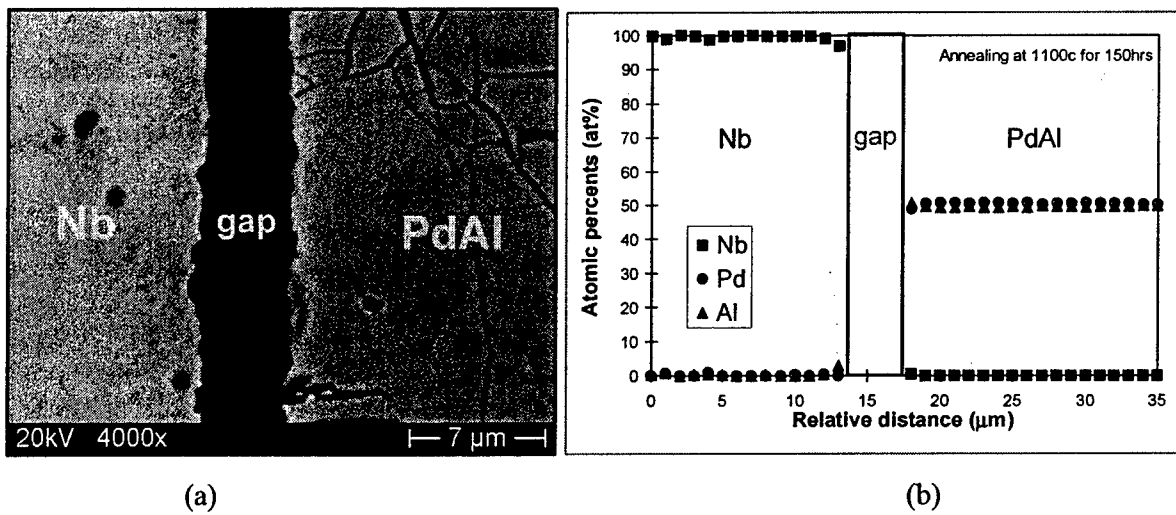


Figure 11. (a) SEM-BSE image of a cross section of the Nb/PdAl diffusion couple annealed at 1100 °C for 150 hours and (b) Nb, Pd and Al concentration profiles obtained from an EPMA line-scanning on the diffusion couple shown in (a).

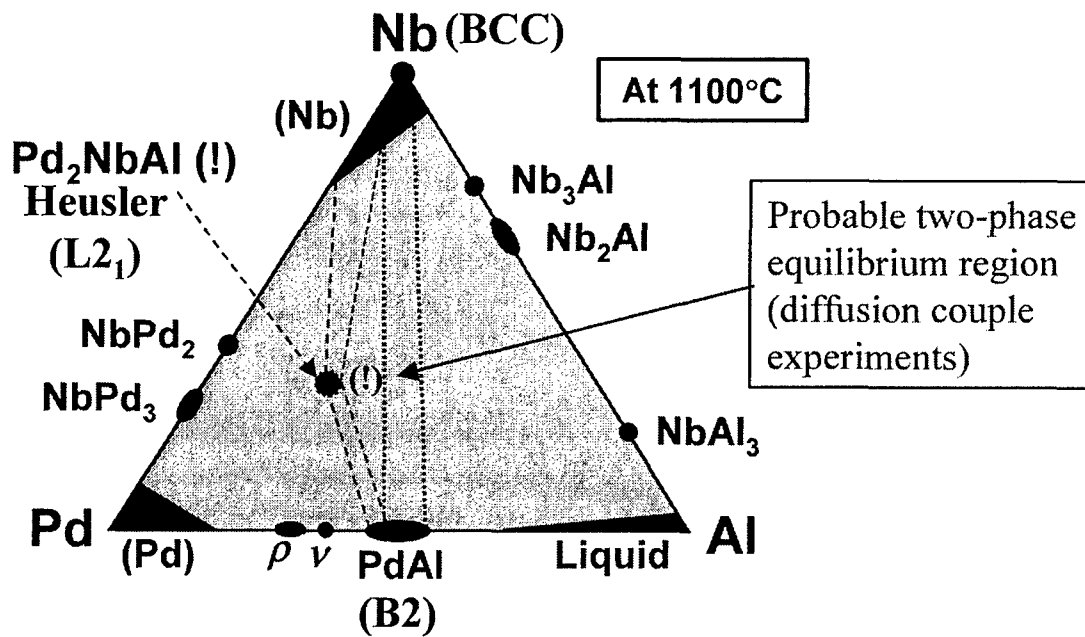


Figure 12. Schematic ternary phase diagram of the Pd-Nb-Al system showing probable three-phase equilibrium among bcc(Nb), B2(PdAl) and L2<sub>1</sub>(Pd<sub>2</sub>NbAl).

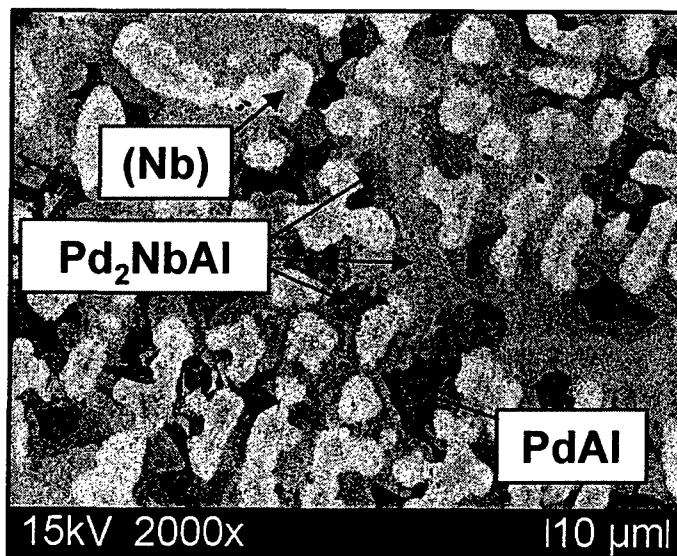


Figure 13. SEM-BSE image of as-cast Pd-25Nb-25Al (at% in unit) alloy showing co-existence of (Nb), PdAl and Pd<sub>2</sub>NbAl.

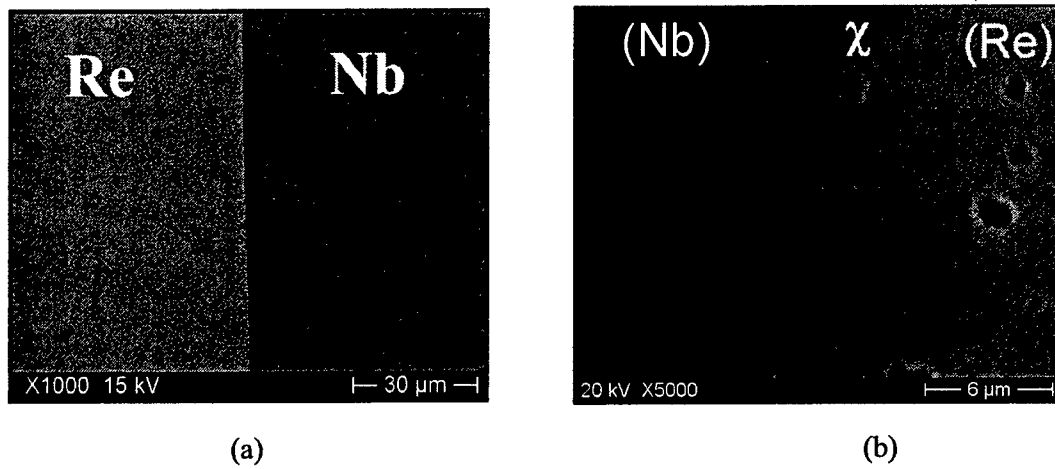


Figure 14. Cross section SEM-BSE image of the Nb/Re diffusion couple annealed at (a) 1100 °C for 200 hours and (b) 1600 °C for 100 hours.

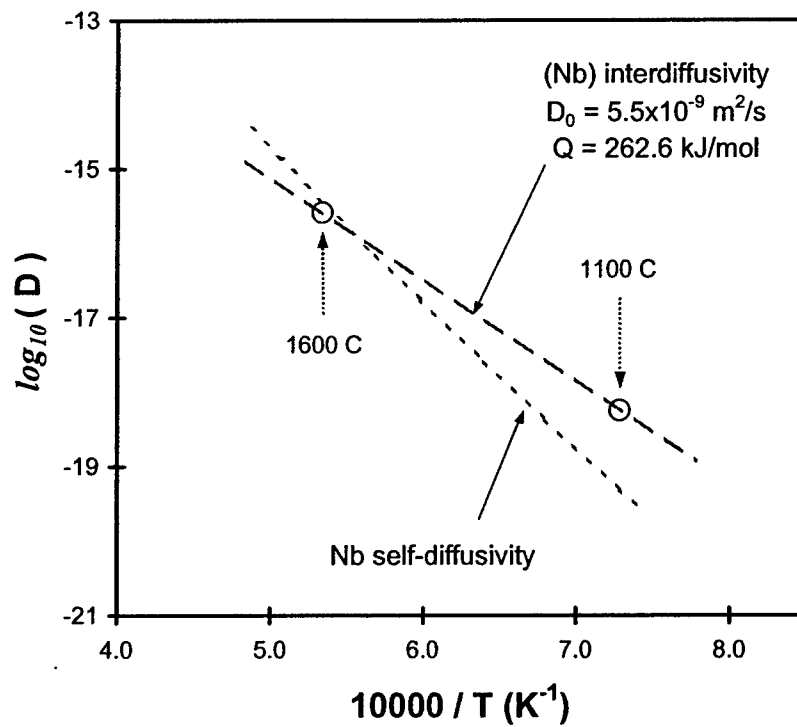
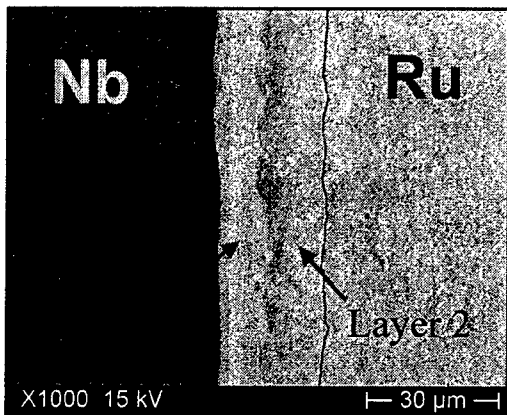
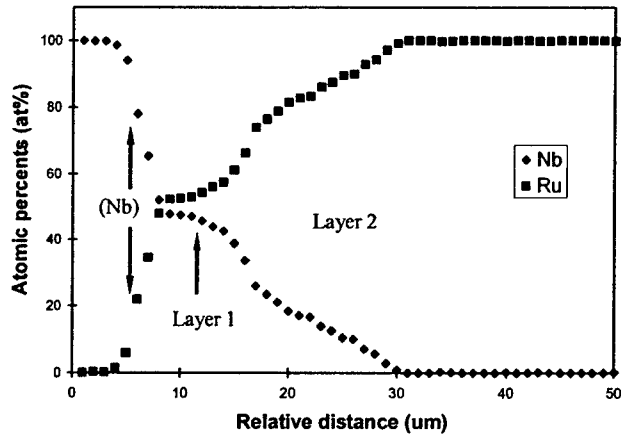


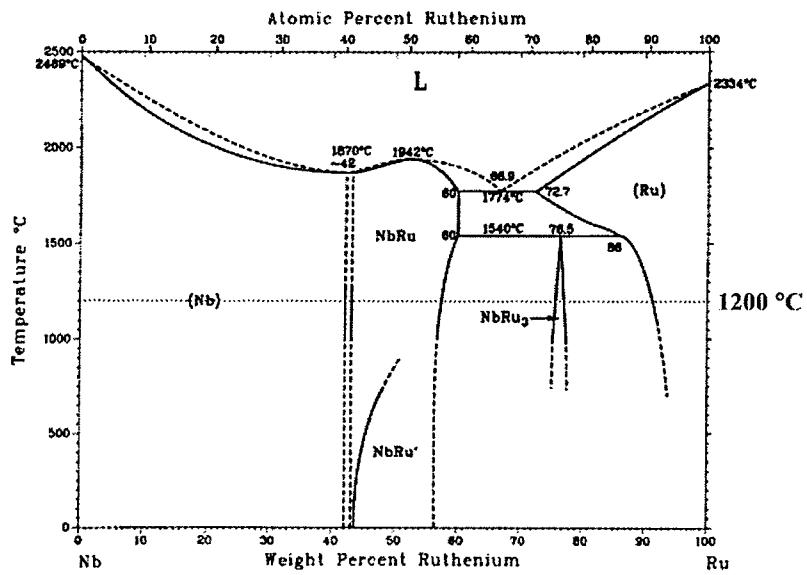
Figure 15. Plot of diffusion coefficients versus reciprocal temperature.



(a)



(b)



(c)

Figure 16. (a) SEM-BSE image of a cross section of the Nb/Ru diffusion couple annealed at 1200 °C for 200 hours, (b) Nb and Ru concentration profiles obtained from an EPMA line-scanning on the diffusion couple shown in (a), and (c) the Nb-Ru binary phase diagram in reference *asm96*.

**REPORT DOCUMENTATION PAGE**

Public reporting burden for this collection of information is estimated to average 1 hour per response, including the time for reviewing instructions, data needed, and completing and reviewing this collection of information. Send comments regarding this burden estimate or any other aspect of this burden to Department of Defense, Washington Headquarters Services, Directorate for Information Operations and Reports (0704-0188), 1215 Jefferson Davis Highway, Suite 1204, Arlington, VA 22202-4302. Respondents should be aware that notwithstanding any other provision of law, no person shall be subject to any penalty for failing to comply with a collection of information if it does not display a currently valid OMB control number. **PLEASE DO NOT RETURN YOUR FORM TO THE ABOVE ADDRESS.**

0260 0259

<b>1. REPORT DATE (DD-MM-YYYY)</b> 05-19-2005		<b>2. REPORT TYPE</b> Final Report		<b>3. DATES COVERED (From - To)</b> 9/1/2001 - 8/31/2004	
<b>4. TITLE AND SUBTITLE</b>  Computational Design of Advanced Aeroturbine Materials: Noburnium Cyberalloy				<b>5a. CONTRACT NUMBER</b> F49620-01-1-0529	
				<b>5b. GRANT NUMBER</b>	
				<b>5c. PROGRAM ELEMENT NUMBER</b>	
<b>6. AUTHOR(S)</b>  Olson, Gregory B., Freeman, Arthur J., Asta, Mark D., Ghosh, Gautam, Eberhart, Mark E., Perepezko, John H.				<b>5d. PROJECT NUMBER</b>	
				<b>5e. TASK NUMBER</b>	
				<b>5f. WORK UNIT NUMBER</b>	
<b>7. PERFORMING ORGANIZATION NAME(S) AND ADDRESS(ES)</b>  Gregory B. Olson Northwestern University 633 Clark Street Evanston, IL 60208-1110				<b>8. PERFORMING ORGANIZATION REPORT NUMBER</b>	
<b>9. SPONSORING / MONITORING AGENCY NAME(S) AND ADDRESS(ES)</b> Air Force Office of Sponsored Research 801 North Randolph Street Room 732 Arlington VA 22203-1977				<b>10. SPONSOR/MONITOR'S ACRONYM(S)</b> AFOSR	
				<b>11. SPONSOR/MONITOR'S REPORT NUMBER(S)</b>	
<b>12. DISTRIBUTION / AVAILABILITY STATEMENT</b>  Approved for public release; distribution is unlimited.					
<b>13. SUPPLEMENTARY NOTES</b>					
<b>14. ABSTRACT</b> Under the AFOSR-MEANS initiative, an optimal combination of electronic-level first-principles calculations and efficient experimentation addresses the accelerated design and development of a new class of Nb-based aeroturbine superalloys.					
<b>15. SUBJECT TERMS</b>					
<b>16. SECURITY CLASSIFICATION OF:</b>			<b>17. LIMITATION OF ABSTRACT</b>  Unlimited	<b>18. NUMBER OF PAGES</b>  42	<b>19a. NAME OF RESPONSIBLE PERSON</b> Gregory B. Olson
<b>a. REPORT</b> Unclassified	<b>b. ABSTRACT</b> Unclassified	<b>c. THIS PAGE</b> Unclassified			<b>19b. TELEPHONE NUMBER (include area code)</b> (847) 491-2847